at the baseline (I_b) and at the follow up (I_f) (Fotenos *et al.*, 2005).

$$\text{Atrophy rate} = \frac{(I_b - I_f)}{I_b}$$

Images of the atrophy rate were smoothed using a 8 mm full-width half-maximum of an isotropic Gaussian kernel.

For the present analysis, we took the severity of WMH into consideration. The levels for overall severity of white matter excluding B&T were divided into four: 0, no lesion; 1, focal lesions in at least one lobe; 2, beginning confluence of lesions in at least one lobe; 3, diffuse lesions in all over white mattes (Figure 1), and 0, no lesion; 1, focal lesions; 2, >1 focal lesions, and 3, confluent lesions for B&T (DeCarli *et al.*, 2005).

Two trained operators rated the overall severity for white matter excluding B&T and the severity of B&T of the 84 participants, and the reproducibility was calculated. The intra-class correlation coefficients (ICCs) for these measurements were 0.85 and 0.95, respectively. ICC values over 0.75 indicate good reliability, so our rating is considered to be reliable (Landis and Koch, 1977).

The relationship between the atrophy rate of regional gray matter volume and the severity of WMH at the baseline scan was evaluated using a single regression model. Only correlations that had a cluster level of $p < 0.001$ (uncorrected) with an extent threshold criterion of more than 300 contiguous voxels were considered statistically to be significant. For the evaluation of the effect of WMH on the gray matter volume, the result was masked with the gray matter image derived from the WFU_pickatlas (Maldjian *et al.*, 2003). Subsequently, we evaluated the correlation between severity of the WMH and progression of the brain atrophy using age as a nuisance variable. We regarded the criteria same as above (a cluster level of $p < 0.001$ (uncorrected) with an extent threshold criterion of more than 300 contiguous voxels) as statistically significant, too. Only this process, statistical analysis was performed using SPM2.

We also evaluated the differences among the four levels (Fazekas = 0, 1, 2, and 3) according to age, sex, MMSE score, years of education, and scan interval using one-way ANOVA. Statistical analyses were performed using SPSS for Windows 11.0.1J software (SPSS Japan, Tokyo, Japan).

Results

The first analysis for the 74 subjects lacking hyperintensities in B&T showed significant positive correlations between the atrophy rate of regional gray matter and severity of WMH in the bilateral parietal and occipital cortices axisymmetrically, birateral precentral gyri, and right frontal cortex (Figure 2). The analyses showed no significant difference in sex, MMSE score, years of education, and scan interval among the four groups. However, only a significant difference in age

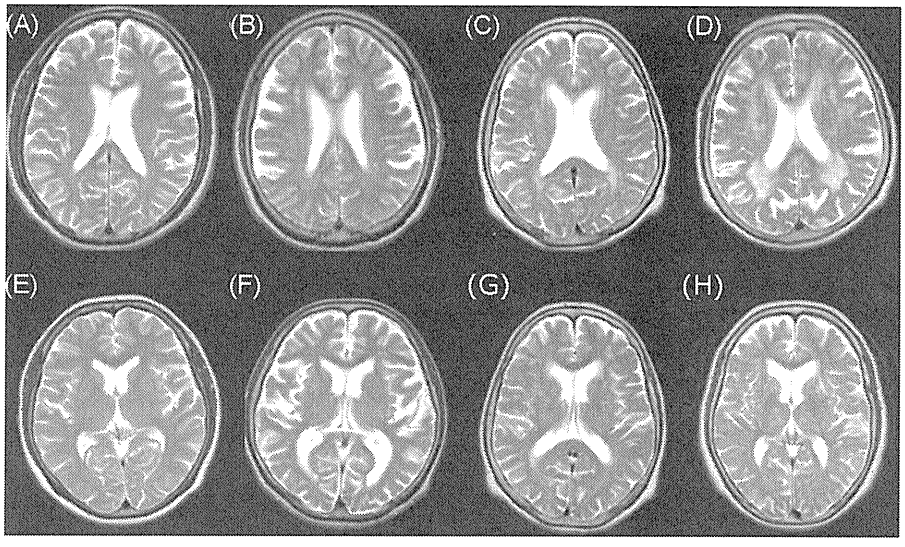

Figure 1 (A–H) Examples of rating scores 0, 1, 2, and 3 on cerebral T2-weighted imaging. Upper column: definitions of rating scores for white matter lesions: 0, no lesion (A); 1, focal lesions (B); 2, beginning confluence of lesions (C); 3, diffuse lesions in all over white mattes (D). Lower column: definitions of rating scores for basal ganglia and thalami: 0, no lesion (E); 1, focal lesions (F); 2, >1 focal lesions (G), and 3, confluent lesions (H).

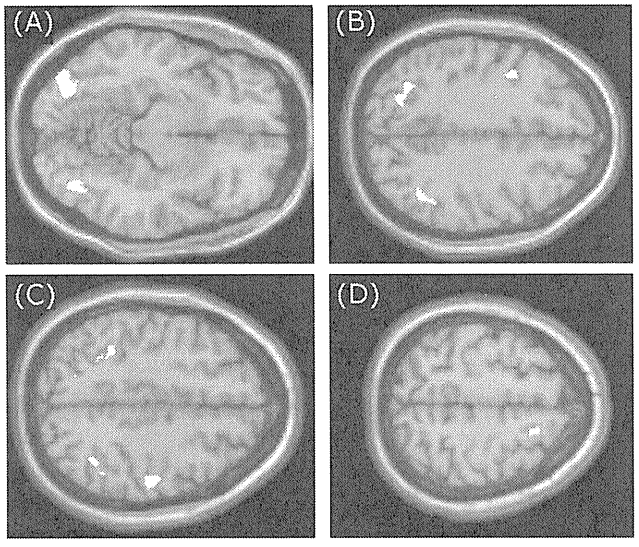

Figure 2 The relationship between the atrophy rate of regional gray matter volume and WMH severity at the baseline scan was evaluated in 74 participants without the hyperintensity in basal ganglia (single regression model, SPM5). There were positive correlations between WMH severity and the atrophy rate of the regional gray matter volume of (A) the bilateral occipital corti, (B) the bilateral parietal corti and left precentral gyrus, (C) the right precentral gyrus, and (D) right frontal cortex.

was observed between groups with Fazekas = 0 and Fazekas = 2 groups. Further, the subsequent analysis evaluating the correlation between severity of the WMH and atrophy rate using age as a nuisance variable showed significant positive correlations between the atrophy rate of regional gray matter and severity of WMH in the bilateral parietal and occipital cortices nearly axisymmetrically (Figure 3).

The second analysis using the data from 13 participants with hyperintensities in B&T showed only a slightly positive correlation between severity of WMHs and the atrophy rate of regional gray matter in the left parietal gyrus at the trend level (Figure 4; a seed level of $p < 0.01$ (uncorrected)).

In sum, the first analysis showed fairly axisymmetrical pattern, while the findings gained from the second analysis appear to lack systematic orderliness.

Discussion

The first analysis showed significantly positive correlations between the atrophy rate of gray matter and the severity of WMH at the baseline scan in the bilateral frontal, occipital and parietal lobes almost axisymmetrically (Figure 2). However, the second did not replicate the findings.

Previous studies showed that WMHs in any brain region cause other cortical changes (Tullberg *et al.*, 2004; Rossi *et al.*, 2006; Wen *et al.*, 2006). In addition, a study showed that there were correlations not only between WMH volume in each subdivided region and WMH volume for the overall brain, but also among each WMH volume in subdivided regions, respectively (DeCarli *et al.*, 2005). On the other hand, there are too many factors involved in the interaction to evaluate the relationship between the atrophy and the WMHs. Therefore, for the simplicity purpose, we regarded the severity of WMH for overall brain as the individual index for the subcortical WMH severity.

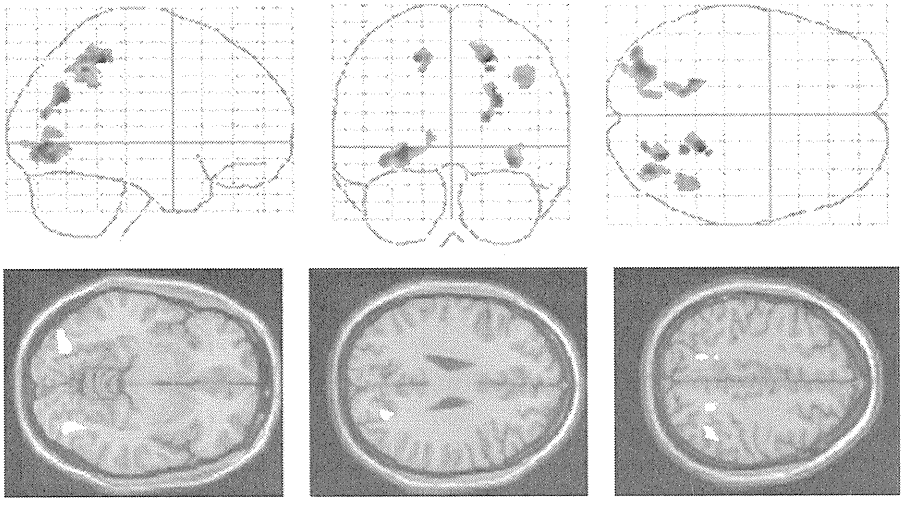

Figure 3 The relationship between the atrophy rate of regional gray matter volume and WMH severity at the baseline scan using the age as nuisance variable was evaluated in 74 participants without the hyperintensity in basal ganglia (SPM2). There were positive correlations between WMH severity and the atrophy rate of the regional gray matter volume of the bilateral occipital and parietal corti.

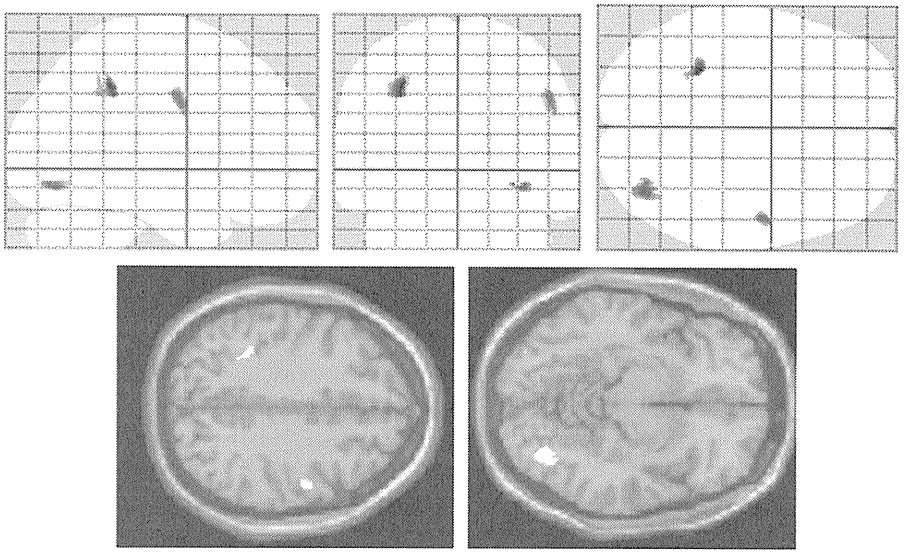

Figure 4 There was a positive correlation between severity of hyperintensity and the atrophy rate of regional gray matter volume of the left parietal cortex at the trend level in 13 participants with the severe hyperintensity in basal ganglia and thalamus.

Our results showing the relationship between the severity of WMH and the atrophy rate is compatible with previous result in general. It is known that WMH loads are likely to be observed in the white matter around the frontal horn of the lateral cerebral ventricle in the frontal lobes, and the posterior horn of the lateral cerebral ventricle in the parieto-occipital lobes, and WMH were distributed symmetrically (Wahlund *et al.*, 2001; Yoshita *et al.*, 2006). Others showed that frontal and parieto-occipital regions are the most common sites for WMH (Tullberg *et al.*, 2004; Rossi *et al.*, 2006). Our study duplicated such distribution pattern of WMH. Our result of the cerebral shrinkage and the severity of whole brain WMH might be mainly explained by the correlation between the shrinkage of the cortex in the frontal, parietal, and occipital lobes and the severity of WMH in their respective lobes. Further, the additional analysis evaluating the relationship between the severity of the WMH and atrophy rate without the aging effect showed significant positive correlations between the atrophy rate of gray matter and the severity of WMH in the bilateral occipital and parietal lobes axisymmetrically, but not in frontal regions. These fingins showed in occipito-parietal regions were nearly the same as the results not excluding the aging effect. Aging disproportionately affects frontal lobe structure, and leaving posterior and inferior brain regions relatively intact (Pfefferbaum *et al.*, 2005). In this regard, the confounding factor, aging effect, may affect these viewpoints.

Hyperintensities in the B&T mediating vast communication over widespread areas of the cortex (Mungas *et al.*, 2005; Leh *et al.*, 2007) might induce volume change in not only the brain structures *per se*, but also the connected cerebral cortices. However, previous studies paid little attention to the hyperintensities in B&T, and these results not always indicate axisymmetrical correlation. In this point, our study is the first one that investigated the WMH and cortical volume with attention to the presence or absence of the hyperintensities in B&T. When considering B&T mediate vast communication over widespread cortex (Behrens *et al.*, 2003; Mungas *et al.*, 2005), hyperintensities in B&T might induce volume change in not only the brain structures *per se*, but also the connected cerebral cortices. The second analysis using the data from 13 subjects with hyperintensities in B&T showed the asymmetrical relationship between the atrophy rate and the WMH severity. Thus, the differences in the results may be attributable to the influence of the hyperintensities in B&T.

There is a limitation in this study. First, T2 images were acquired with slice thickness of 5 mm and gap of 1.5 mm. Although our participants showed no large ischemic lesion in B&T, it might be possible that WMH from small brain structures such as thalamus and basal ganglia may not be observed. Further work using thin slice thickness and gapless T2 image will be necessary to confirm our results. Second, we did not have a large enough number of subjects with WMH loads in the basal ganglia and thalami. The procedure to extract cognitively healthy subjects through several tests might have excluded or limited the subjects with WMH lesions, which affect cognitive ability. Further studies using a large group of subjects need to be conducted. Third, previous study showed the different efficacy

Key points

- We showed fairly axisymmetrical atrophy pattern in subjects without the hyperintensities in basal ganglia and thalami.
- The atrophy pattern of the cerebrum with the subjects with the hyperintensities in basal ganglia and thalami appear to lack systematic orderliness.
- This result shows that WMH may affect atrophy in multiple cerebral cortices even in cognitively normal subjects.

of the deep white matter hyperintensity and periventricular white matter hyperintensity on the brain atrophy (Wen *et al.*, 2006), and a fluid-attenuated inversion recovery (FLAIR) sequence may be more useful for assessment of WMH (DeCarli *et al.*, 2005). However, Fazekas = 3 group sometimes showed the contiguous white matter lesion from periventricular space to the deep white matter, and the number of Fazekas = 3 group were relatively small. So, we could not divide these findings. Further works concerning this point using the same method will be necessary. In addition, we evaluated the severity of WMH by qualitative method, not by quantitative one, and the previous study showed that the periventricular WMH and deep white matter hyperintensities were highly correlated with total WMH and with each other (DeCarli *et al.*, 2005). Consequently, we managed to show the statistically significant correlations. Further studies using a FLAIR sequence need to be conducted.

In conclusion, WMH are associated with shrinkage of every lobe even in cognitively normal subjects. Understanding the impact of WMH on the shrinkage shown in the brains of cognitively healthy older individuals is an important base for assessing the temporal pattern of atrophy of the individual with neurodegenerative disorder including AD.

Conflicts of interest

None declared.

References

Adachi T, Kobayashi S, Yamaguchi S. 2002. Frequency and pathogenesis of silent subcortical brin infactiono ain acute first-ever ischemic stroke. *Intern Medicine* **41**: 103–108.

Behrens TE, Johansen-Berg H, Woolrich MW, *et al.* 2003. Non-invasive mapping of connections between human thalamus and cortex using diffusion imaging. *Nat Neurosci* **6**: 750–757. [Pubmed: 12808459].

Brodaty H, Moore CM. 1997. The Clock Drawing Test for dementia of the Alzheimer's type: a comparison of three scoring methods in a memory disorders clinic. *Int J Geriatr Psychiatry* **12**: 619–627. [Pubmed: 9215942].

DeCarli C, Fletcher E, Ramey V, *et al.* 2005. Anatomical mapping of white matter hyperintensities (WMH): exploring the relationships between periventricular WMH, deep WMH, and total WMH burden. *Stroke* **36**: 50–55. [Pubmed: 15576652].

De Reuck J, Decoo D, Strijckmans K, *et al.* 1992. Does the severity of leukoaraiosis contribute to senile dementia? A comparative computerized and positron emission tomographic study. *Eur Neurol* **32**: 199–205. [Pubmed; 1505589].

Du AT, Schuff N, Chao LL, *et al.* 2005. White matter lesions are associated with cortical atrophy more than entorhinal and hippocampal atrophy. *Neurobiol Aging* **26**: 553–559. [Pubmed: 15653183].

Fotenos AF, Snyder AZ, Girton LE, *et al.* 2005. Normative estimates of cross-sectional and longitudinal brain volume decline in aging and AD. *Neurology* **64**: 1032–1039. [Pubmed: 15781822].

Good CD, Johnsrude I, Ashburner J, *et al.* 2001. Cerebral asymmetry and the effect of sex and handedness on brain structure: a voxel-based morphometric analysis of 465 normal adult human brains. *Neuroimage* **4**: 685–700. [Pubmed: 11506541].

Grober E, Buschke H, Crystal H, *et al.* 1998. Screening for dementia by memory testing. *Neurology* **38**: 900–903. [Pubmed: 3368071].

Junqué C, Pujol J, Vendrell P, *et al.* 1990. Leukoaraiosis on magnetic resonance imaging and speed of mental processing. *Arch Neurol* **47**: 151–156. [Pubmed: 2302086].

Landis JR, Koch GG. 1977. The measurement of observer agreement for categorical data. *Biometrics* **33**: 159–174. [Pubmed: 843571].

Leh SE, Ptito A, Chakravarty MM, *et al.* 2007. Fronto-striatal connections in the human brain: a probabilistic diffusion tractography study. *Neurosci Lett* **419**: 113–118. [Pubmed: 17485168].

Maldjian JA, Laurienti PJ, Burdette JB, *et al.* 2003. An automated method for neuroanatomic and cytoarchitectonic atlas-based interrogation of fMRI data sets. *NeuroImage* **19**: 1233–1239. [Pubmed: 12880848].

Mirsen TR, Lee DH, Wong CJ, *et al.* 1991. Clinical correlates of white-matter changes on magnetic resonance imaging scans of the brain. *Arch Neurol* **48**: 1015–1021. [Pubmed: 1929891].

Misra C, Fan Y, Davatzikos C. 2009. Baseline and longitudinal patterns of brain atrophy in MCI patients, and their use in prediction of short-term conversion to AD: results from ADNI. *Neuroimage* **44**: 1415–1422. [Pubmed: 19027862].

Miyamoto M, Kodama C, Kinoshita T, *et al.* 2009. The issue of non-responders: comparison of the prevalence of dementia and mild cognitive impairment among quick-, delayed-responders, and final-nonresponders to a community survey. *J Clin Neurosci* **16**: 270–276. [Pubmed: 19091575].

Monsch AU, Bondi MW, Butters N, *et al.* 1992. Comparisons of verbal fluency tasks in the detection of dementia of the Alzheimer type. *Arch Neurol* **49**: 1253–1258. [Pubmed: 1449404].

Mungas D, Harvey D, Reed BR, *et al.* 2005. Longitudinal volumetric MRI change and rate of cognitive decline. *Neurology* **65**: 561–571. [Pubmed: 16116117].

Ogawa T, Yoshida Y, Okudera T, *et al.* 1997. Secondary thalamic degeneration after cerebral infarction in the middle cerebral artery distribution: evaluation with MR imaging. *Radiology* **204**: 255–262. [Pubmed: 9205256].

Ota M, Obata T, Akine Y, *et al.* 2007. Laterality and aging of thalamic subregions measured by diffusion tensor imaging. *Neuroreport* **18**: 1071–1075. [Pubmed: 17558299].

Pfefferbaum A, Adalsteinsson E, Sullivan EV. 2005. Frontal circuitry degradation marks healthy adult aging: evidence from diffusion tensor imaging. *Neuroimage* **26**: 891–899. [Pubmed: 15955499].

Rossi R, Boccardi M, Sabattoli F, *et al.* 2006. Topographic correspondence between white matter hyperintensities and brain atrophy. *J Neurol* **253**: 919–927. [Pubmed: 16502217].

Sasaki M, Kodama C, Hidaka S, *et al.* 2009. Prevalence of four subtypes of mild cognitive impairment and APOE in a Japanese community. *Internat J Geriat Psychiat* **24**: 1119–1126. [Pubmed: 19449451].

Scheltens P, Barkhof F, Valk J, *et al.* 1992. White matter lesions on magnetic resonance imaging in clinically diagnosed Alzheimer's disease. Evidence for heterogeneity. *Brain* **115**: 735–748. [Pubmed: 1628199].

Schmidt T, Fazekas F, Offenbacher H, *et al.* 1993. Neuropsychologic correlates of MRI white matter hyperintensities: a study of 150 normal volunteers. *Neurology* **43**: 2490–2494. [Pubmed: 8255445].

Smith EE, Egorova S, Blacker D, *et al.* 2008. Magnetic resonance imaging white matter hyperintensities and brain volume in the prediction of mild cognitive impairment and dementia. *Arch Neurol* **65**: 94–100. [Pubmed: 18195145].

Sohlberg MM, Mateer CA. 1986. *Attention Process Training (APT)*. Association for Neuropsychological Research and Development: Puyallup, WA.

Tullberg M, Fletcher E, DeCarli C, *et al.* 2004. White matter lesions impair frontal lobe function regardless of their location. *Neurology* **63**: 246–253. [Pubmed; 15277616].

Wahlund LO, Barkhof F, Fazekas F, *et al.* 2001. European Task Force on age-related white matter changes. A new rating scale for age-related white matter changes applicable to MRI and CT. *Stroke* **32**: 1318–1322. [Pubmed: 11387493].

Wechsler D. 1981. *WAIS-R Manual*. The Psychological Corporation: New York.

Wen W, Sachdev P, Chen X, *et al.* 2006. Gray matter reduction is correlated with white matter hyperintensity volume: a voxel-based morphometric study in a large epidemiological sample. *Neuroimage* **29**: 1031–1039. [Pubmed: 16253521].

Yoshita M, Fletcher E, Harvey D, *et al.* Extent and distribution of white matter hyperintensities in normal aging, MCI, and AD. *Neurology* 2006. **67**: 2192–2198. [Pubmed: 17190943].

Neuroradiology (2011) 53:3–11
DOI 10.1007/s00234-010-0684-7

DIAGNOSTIC NEURORADIOLOGY

Brachial and lumbar plexuses in chronic inflammatory demyelinating polyradiculoneuropathy: MRI assessment including apparent diffusion coefficient

Yuko Adachi · Noriko Sato · Tomoko Okamoto · Masayuki Sasaki · Hirofumi Komaki · Fumio Yamashita · Jiro Kida · Tomoyuki Takahashi · Hiroshi Matsuda

Received: 21 December 2009 / Accepted: 11 March 2010 / Published online: 20 April 2010

Abstract
Introduction Our purpose was to clarify the magnetic resonance (MR) imaging characteristics of the brachial and lumbar plexuses in patients with chronic inflammatory demyelinating polyradiculoneuropathy (CIDP) using various kinds of sequences, including diffusion-weighted images (DWI).
Methods We evaluated the MR imaging findings for lumbar and/or brachial nerve plexuses in 13 CIDP patients and 11 normal volunteers. The nerve swelling was evaluated in comparison with normal controls by coronal short tau inversion recovery (STIR), and signal abnormalities were evaluated by coronal STIR, T1-weighted images, and DWIs. The degrees of contrast enhancement and apparent diffusion coefficient (ADC) values of the plexus were also assessed.
Results In the patient group, diffuse enlargement and abnormally high signals were detected in 16 out of 24 plexuses (66.7%) on STIR, a slightly high signal was detected in 12 of 24 plexuses (50%) on T1-weighted images, and a high-intensity signal was detected in 10 of 18 plexuses (55.6%) on DWIs with high ADC values. Contrast enhancement of the plexuses was revealed in 6 of 19 plexuses (31.6%) and was mild in all cases. There were statistically significant differences between the ADC values of patients with either swelling or abnormal signals and those of both normal volunteers and patients without neither swelling nor abnormal signals. There were no relationships between MR imaging and any clinical findings.
Conclusion STIR is sufficient to assist clinicians in diagnosing CIDP. T1-weighted images and DWIs seemed useful for speculating about the pathological changes in swollen plexuses in CIDP patients.

Keywords Chronic inflammatory demyelinating polyradiculoneuropathy · Peripheral nerve · Diffusion-weighted MRI · Apparent diffusion coefficient · Onion bulb

Y. Adachi · N. Sato (✉) · F. Yamashita · J. Kida · T. Takahashi
Department of Radiology,
National Center Hospital of Neurology and Psychiatry,
4-1-1 Ogawahigashi-cyo,
Kodaira, Tokyo 187-8511, Japan
e-mail: snoriko@ncnp.go.jp

T. Okamoto
Department of Neurology,
National Center Hospital of Neurology and Psychiatry,
4-1-1 Ogawahigashi-cho,
Kodaira, Tokyo 287-8511, Japan

M. Sasaki · H. Komaki
Department of Child Neurology,
National Center Hospital of Neurology and Psychiatry,
4-1-1 Ogawahigashi-cho,
Kodaira, Tokyo 287-8511, Japan

H. Matsuda
Department of Nuclear Medicine,
Saitama Medial University Hospital,
38 Morohongo, Moroyama-cho,
Iruma-gun, Saitama 350-0495, Japan

Introduction

Chronic inflammatory demyelinating polyradiculoneuropathy (CIDP) is an acquired peripheral neuropathy of presumed autoimmune etiology, which is either a chronically progressive or relapsing–remitting disorder [1]. The

major symptoms are bilateral proximal and distal limb muscle weakness and sensory loss. Motor deficits are usually predominant. This disease commonly affects brachial or lumbar plexuses distributed in the muscles of the extremities. Cranial or diaphragmatic nerve involvement is rarely seen. The involved peripheral nerves in CIDP reveal a unique pathological finding. They are grossly enlarged due to proliferation of surrounding Schwann cells, causing an "onion bulb" appearance [1], although the axons are usually preserved.

A diagnosis of CIDP is generally based on clinical features and electrophysiological studies. As the disease has been studied in various clinical trials, several clinical definitions of this neuropathy have been proposed [2–4]. Cerebrospinal fluid examination, nerve biopsy, and magnetic resonance (MR) examinations provide supportive information but are not always required for diagnosis. However, demonstrable MR imaging findings have been reported, and they are helpful for diagnosis.

Several studies have described the MR imaging findings of CIDP patients. Swelling brachial or lumbar plexuses with increased signal intensity on T2-weighted images with or without contrast enhancement have been reported [5–9]. Coronal short tau inversion recovery (STIR) imaging is particularly helpful for depicting the signal abnormalities of brachial and lumbar plexuses [6]. However, no original reports have evaluated either the diffusion property in patients with CIDP or the T1-weighted images obtained before gadolinium administration, although the contrast enhancement pattern of the nerve plexus has been examined [5, 6].

In this study, we evaluated MR imaging findings of the brachial or lumbar plexus in patients with CIDP using STIR, T1-weighted images before and after contrast enhancement, and diffusion-weighted MRI (DWI), along with the calculation of apparent diffusion coefficient (ADC) values. The aim of this study was to demonstrate the MR imaging findings including some new sequences and to clarify the role of the MR examination in supporting the diagnosis of CIDP.

Materials and methods

Patients

The subjects included 13 consecutive patients (five males and eight females, ranging in age from 5 to 85 years old, mean age±SD; 45.2±25.0 years) who consulted our hospital from 2004 to 2007 and agreed to undergo an MR imaging examination. MR images of all 13 patients with CIDP were retrospectively reviewed. The patients all met the clinical and neurophysiological criteria for CIDP (Joint Task Force of the EFNS and PNS) [2]. No other cause of the neuropathy was found in clinical, laboratory, or histological investigations. None of the patients had a history of exposure to neurotoxic agents or a family history of neuropathy. Disease duration at the time of the MR studies ranged from 6 months to 20 years (mean±SD; 5.0± 6.2 years). Eleven patients had the relapsing–remitting form of the disease and two had the progressive form (cases 3 and 7). In eight patients, no treatment was administered before the MR study. In two patients (cases 1 and 4), immunoglobulin was administered before the MR examination because Guillain–Barre syndrome had been one of their possible diagnoses. The remaining three patients (cases 5, 8, and 10) had long disease duration, and both immunoglobulin and corticosteroid therapy had already been administered before the MR studies. The F wave, which indicated motor conduction along the entire peripheral axon including the radicular segment, was examined as an electrodiagnostic study in all patients. The median nerve conduction was measured at the wrist, and the tibial nerve conduction was measured at the ankle. In one patient, a biopsy was performed at the sural nerve with pathological confirmation of CIDP.

MR studies were also performed in 11 normal volunteers (six males and five females) as a control group. Their ages ranged from 22 to 73 years (mean±SD; 56.5±16.7 years). This study had appropriate Ethics Committee approval.

Imaging

MR examinations were performed on a 1.0-T scanner (Harmony; Siemens, Erlangen, Germany) using a spine array coil. MR studies of both cervical and lumbar plexuses were acquired in all but two (cases 4 and 8) of the 13 patients. One of these two (case 8) underwent an MR examination of only the brachial plexuses, and the other underwent that (case 4) of only the lumbar plexus. In total, 24 nerve plexuses in thirteen patients were evaluated. Coronal STIR and fat-saturated T1-weighted images were acquired in all studies. Gadolinium was administered in all but three patients (cases 8, 10, and 11). One patient (case 4) underwent gadolinium administration only in the MR examination of the brachial plexus, not in the study of the lumbar plexus. The other patients underwent gadolinium administration in MR studies of both the brachial and lumbar plexuses. In total, gadolinium was administered in the examinations of 19 nerve plexuses in 10 patients. DWIs were not acquired in four patients (cases 4, 5, 6, and 8), and thus DWIs were obtained in examinations of 18 nerve plexuses in nine patients.

Follow-up MR studies were carried out in two patients. One patient (case 9) underwent MR studies three times over 8 months: before treatment, after treatment, and during the

relapse phase. In another patient (case 1), a follow-up MR study was performed 1 year after the first study, although he had no clinical symptoms.

Among the 11 normal volunteers, MR studies of both the cervical and lumbar plexuses were carried out in two cases, of only the brachial plexus in five cases, and of only the lumbar plexus in four cases. In total, 13 plexuses were evaluated. Coronal STIR, fat-saturated T1-weighted images, and DWIs were obtained in all normal volunteers. Gadolinium administration was not performed.

The parameters of the coronal STIR sequence were as follows: repetition time/echo time/inversion time [TR/TE/TI], 4,210/85/150; 4-mm sections without gaps; fields of view [FOV], 260×260 (brachial plexus), 280×280 (lumbar plexus); imaging matrix, 512×512; number of excitations (NEX), 1. The parameters of the coronal fat-saturated T1-weighted image sequence before and after gadolinium administration were [TR/TE]=1,330/16; 3-mm sections without gaps; FOV, 260×260 (brachial plexus), 280×280 (lumbar plexus); imaging matrix, 512×512, NEX, 2. The DWIs were obtained using an axial single-shot spin-echo echo-planar imaging sequence with the following parameters: [TR/TE/TI], 10,000.0/86.0/150; 4-mm sections without gaps; FOV, 400×400 (brachial and lumbar plexus); imaging matrix, 256×256; and NEX, 3. Motion-probing gradients were applied in six directions (*xx*, *yy*, *zz*, *xy*, *xz*, and *yz*) with *b* values of 0 and 1,000 s/mm^2. The scan time was 8 min and 20 s in the brachial plexus and 7 min and 40 s in the lumbar plexus. We then performed maximum intensity projection (MIP) for a stack of isotropic DWIs to reconstruct the images rotated around the *z*-axis using software incorporated into the MR system. The isotropic DWIs were generated based on calculated isotropic ADC values.

Image analysis

Imaging assessment in the patient group was based on agreement between two neuroradiologists who reviewed the images in tandem and who were blinded to clinical information regarding neuropathies. Each neuroradiologist made initial evaluations independently, and any disagreements regarding the final conclusion were resolved by consensus.

Swelling of the plexuses was visually assessed on STIR in comparison to the controls. The signal intensity of each plexus was also evaluated on both STIR and T1-weighted images without contrast enhancement and compared to the signal intensity of the controls. We also visually assessed the signal intensity of the plexus on T1-weighted images after contrast enhancement and compared it to the intensity on images taken before contrast enhancement. We established a grading system for the degree of enhancement in the plexuses: moderate enhancement means that the plexuses have stronger enhancement than the ganglions, and mild enhancement means that the plexuses have milder enhancement than the ganglions. DWIs (b=1000) with MIP reconstruction along the long axis of the spine were also assessed by comparison with the controls.

We measured the ADC values of the plexuses on ADC maps. All of the ADC measurements were made using an Aquarius Netstation Ver 1.4 (Tera Recon, San Mateo, CA, USA) by placing freehand circular regions of interest (ROIs) over the plexus on the ADC map. The average ROI was 4±2 mm^2, and the area varied depending on the plexus. ROIs were carefully placed by two trained operators within the plexus to avoid the partial volume effect at three points, and the ADC values were averaged in each lesion. The intra-class correlation coefficient for these measurements was 92.0%. Intra-class correlation coefficient values greater than 0.9 were regarded as excellent, and the results were thus considered reliable. The differences in the ADC values of the plexuses among healthy subjects, patients without neither swelling nor abnormal signals of the plexus, and patients with either swelling or abnormal signals of the plexus were evaluated by analysis of variance. P values less than 0.05 were considered significant.

Using the unpaired t test, we also evaluated the relationships between age at onset and each MR imaging finding, such as nerve swelling, high signal intensity on STIR, T1-weighted images, DWI, and degree of enhancement. Disease duration was also evaluated in the same way. Additionally, the relationships between each MR finding and the clinical findings (motor and sensory symptoms and F wave latency) were evaluated by Fisher's exact test.

Results

Clinical and imaging features

The clinical and MR imaging findings are summarized in Table 1. All patients presented with motor and/or sensory symptoms in both the upper and lower extremities. F wave latencies were prolonged in either the upper or lower extremities or both of all patients, except for two (cases 2 and 5), whose F waves were absent, probably due to severe nerve damage.

Swelling of the brachial and lumbar plexuses was observed in 16 of 24 plexuses (66.7%) on STIR in 9 out of 13 CIDP patients (Figs. 1 and 2). In the patients who underwent both brachial and lumbar MR examinations, either both plexuses were simultaneously swollen or neither was swollen.

High intensity was shown in 16 of 24 plexuses (66.7%) on STIR in 9 out of 13 CIDP patients, and all 16 plexuses were swollen (Fig. 1a). Slightly high intensity was found in

Table 1 Comparison of clinical and MR imaging findings in patients with CIDP.

Case	Age/sex	Clinical findings					MR findings					
		Disease duration (years)	Portion	Motor symptoms	Sensory symptoms	F wave latencies	Swelling of plexus	High intensity on STIR	High intensity on T1-WI	CE	High intensity of DWI	ADC value ($\times 10^{-3}$ mm^2/s)
1	13/M	0.5	B	+	−	Prolonged	+	+	+	−	+	1.91
			L	+	+	Prolonged	+	+	+	−	+	1.96
2	16/F	6	B	+	−	NR	+	+	+	−	+	1.69
			L	+	−	NR	+	+	+	−	+	2.12
3	39/M	4	B	+	+	Prolonged	+	+	+	−	+	1.43
			L	+	−	Normal	+	+	+	−	+	1.26
4	5/F	1	B	+	−	Normal	Not done	Not done	Not done	Not done	Not done	Not done
			L	+	+	Prolonged	+	+	−	−	Not done	Not done
5	46/M	17	B	+	+	NR	+	+	−	+	Not done	Not done
			L	+	+	NR	+	+	−	+	Not done	Not done
6	64/M	3	B	+	−	Prolonged	+	+	+	−	Not done	Not done
			L	+	+	Normal	+	+	+	−	Not done	Not done
7	66/M	2	B	+	−	Prolonged	+	+	+	+	+	1.50
			L	+	+	Normal	+	+	+	+	+	1.18
8	67/F	20	B	+	−	Prolonged	+	+	−	Not done	Not done	Not done
			L	+	−	Prolonged	Not done	Not done	Not done	Not done	Not done	Not done
9	34/M	1	B	+	+	Prolonged	+	+	+	+	+	1.43
			L	+	−	Prolonged	+	+	+	+	+	1.20
10	85/F	10	B	+	+	Normal	−	−	−	Not done	−	0.98
			L	+	−	Prolonged	−	−	−	Not done	−	1.04
11	36/F	2	B	+	+	Prolonged	−	−	−	Not done	−	0.73
			L	+	+	Normal	−	−	−	Not done	−	0.92
12	75/F	4	B	+	−	Prolonged	−	−	−	−	−	0.78
			L	+	−	Prolonged	−	−	−	−	−	0.77
13	42/F	4	B	−	+	Normal	−	−	−	−	−	0.89
			L	−	+	Prolonged	−	−	−	−	−	1.05

Upper extremity normal F wave latency <32 ms; lower extremity normal F wave latency <60 ms; NR = no response due to absent distal F wave

M male, *F* female, *B* brachial plexus, *L* lumbar plexus, *STIR* short tau inversion recovery, *WI* weighted image, *CE* contrast enhancement, *DWI* diffusion-weighted image, *ADC* apparent diffusion coefficient

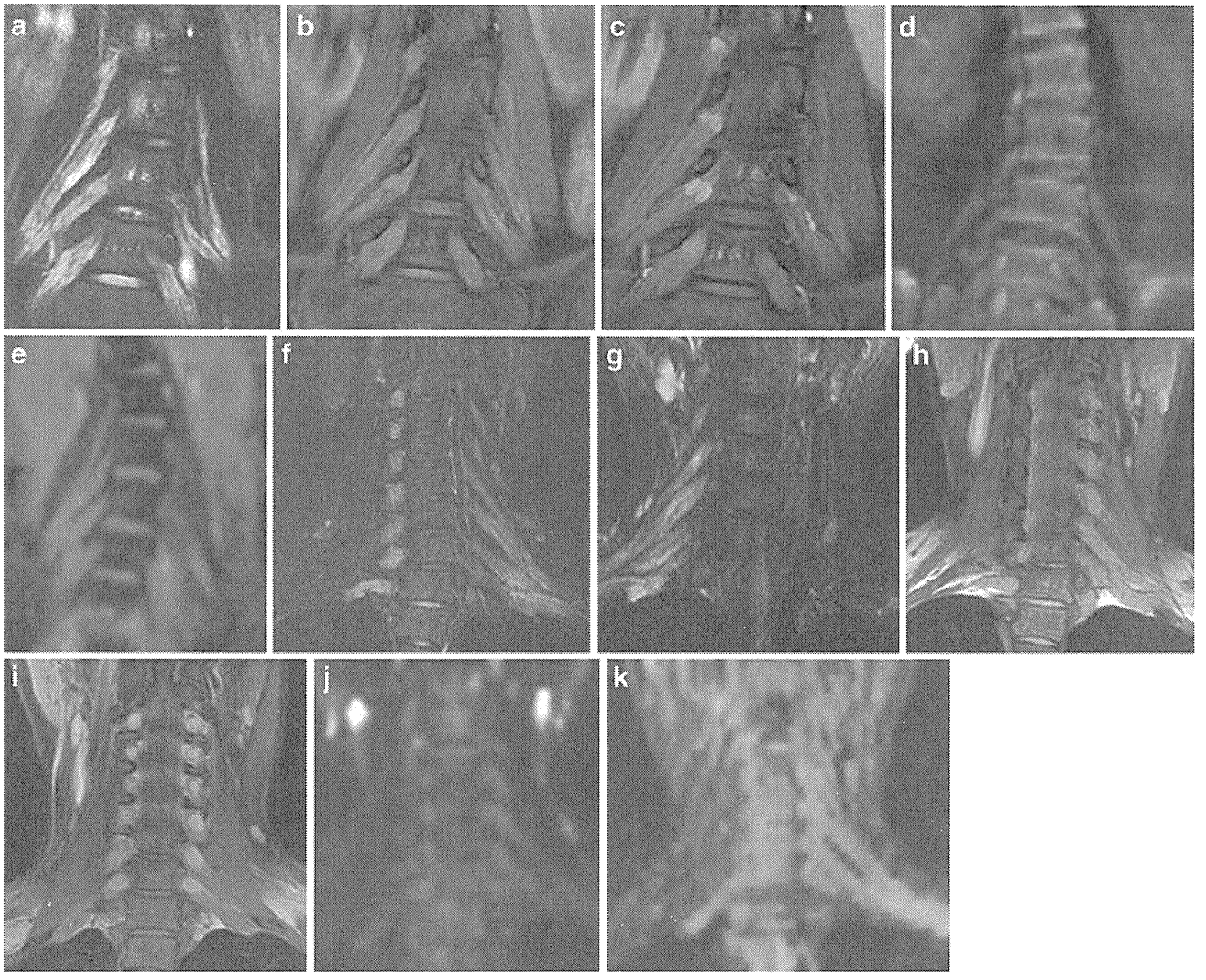

Fig. 1 MR images of a 16-year-old female (case 2 in Table 1) with chronic inflammatory demyelinating polyradiculoneuropathy (CIDP) with symmetrical weakness of both legs and arms for 5 years. **a** Coronal STIR image of the lumbar plexus shows enlargement with a markedly high signal. **b** Lumbar plexus with hypertrophy shows slightly high signal intensity on T1-weighted images without contrast enhancement. **c** T1-weighted images following intravenous gadolinium administration shows an enhancement in the nerve ganglion without enhancement of the lumbar plexus. **d** DWI reconstructed by MIP on the lumbar plexus shows high intensity of the lumbar plexus. **e** ADC map of the lumbar plexus. The ADC value in the lumbar plexus with hypertrophy was 2.1×10^{-3}mm^3/s. **f, g** Coronal STIR reveals hyperintensity and swelling of the bilateral brachial plexus (because this patient had torticollis, both plexuses do not appear in the same slice). **h** Brachial plexus with hypertrophy shows slightly high signal intensity on T1-weighted images. **i** T1-weighted images following intravenous gadolinium administration do not show contrast enhancement of the nerve plexus. **j** DWI demonstrates high signal intensity. **k** The mean ADC value in the brachial plexus was 1.7×10^{-3}mm^3/s

12 of 24 plexuses (50%) on T1-weighted images without contrast enhancement in six patients (Fig. 1b).

Contrast enhancement was shown in 6 of 19 plexuses (31.6%) in 3 out of 10 patients after gadolinium administration (Fig. 2c). All enhanced plexuses showed mild enhancement. In patients who underwent MR studies of both the brachial and lumbar plexuses, either both plexuses were simultaneously enhanced, or neither was enhanced. All enhanced plexuses showed swelling and hyperintensity on STIR.

On DWIs, high intensity was found in 10 of 18 plexuses in 5 out of 9 patients (55.6%); all 10 plexuses showed swelling and high intensity on STIR and slightly high intensity on T1-weighted images before gadolinium administration (Fig. 1a, b, e). The remaining eight plexuses that did not show high intensity on DWIs did not show swelling or high intensity on STIR or on T1-weighted images.

In one patient who was examined three times in total from before to after treatment (case 9), all MR findings such as swelling, signals in all sequences, and contrast

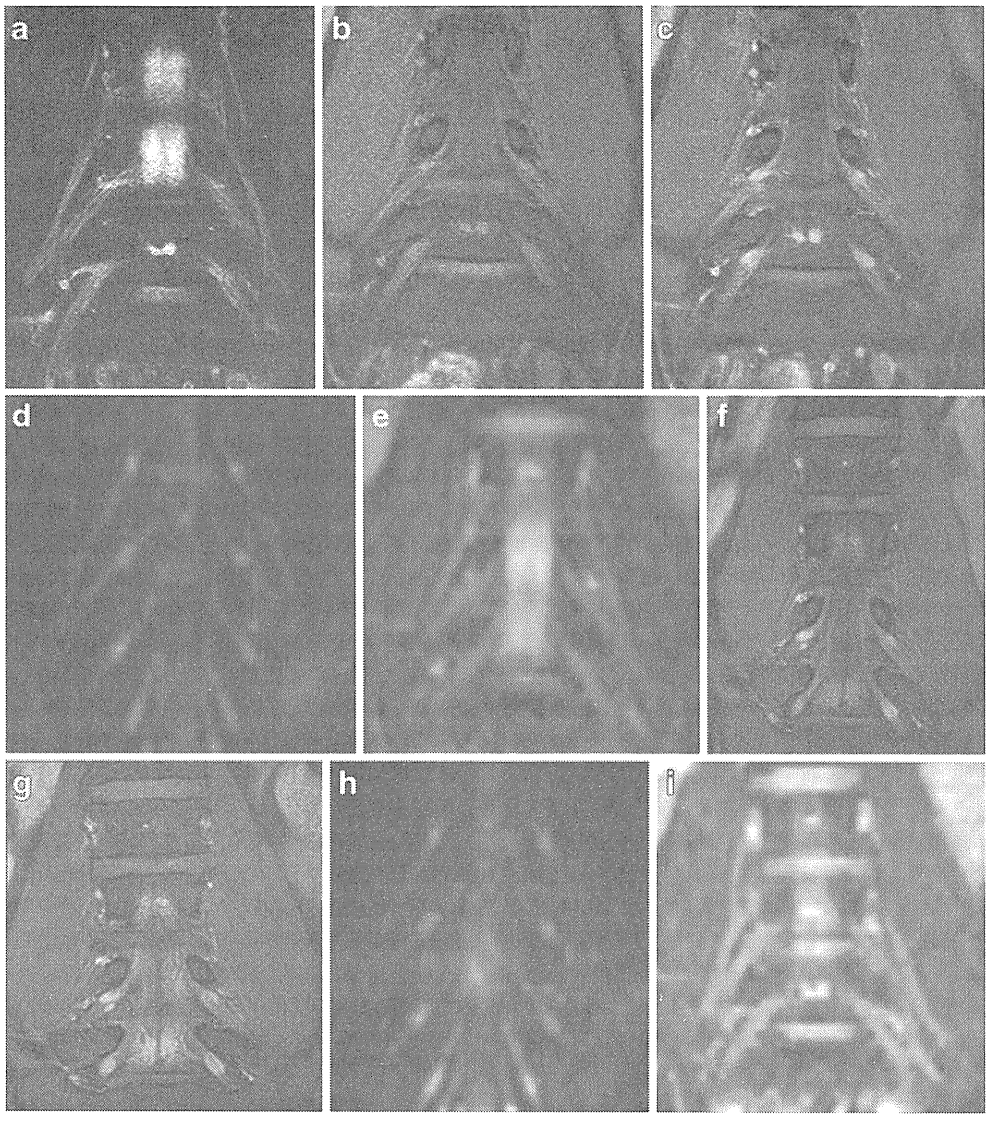

Fig. 2 MR images from a 34-year-old man (case 9 in Table 1) with CIDP, with a 6-month history of weakness in both legs and arms as well as sensory loss in the arms. **a** Coronal STIR image reveals moderate swelling and hyperintensity of the lumbar plexus bilaterally. **b** Lumbar plexus with hypertrophy shows slightly high signal intensity on T1-weighted image. **c** T1-weighted image following intravenous gadolinium administration shows mild enhancement in the lumbar plexus. **d** DWI reconstructed by MIP on the lumbar plexus demonstrates high intensity. **e** ADC map of the lumbar plexus. The ADC value was 1.5×10^{-3} mm^3/s. **f** T1-weighted images with gadolinium obtained 1 month after immunoglobulin therapy; the degree of enhancement is unchanged. **g** T1-weighted image with gadolinium obtained at the relapse phase, 6 months after immunoglobulin therapy; the degree of enhancement is unchanged. **h** DWI reconstructed by MIP on the lumbar plexus after treatment obtained at the same time as **g** shows no remarkable changes in the intensity of the lumbar plexus. **i** ADC map of the lumbar plexus. The ADC value was $1.5\times10^{-3}mm^3/s$

enhancement remained unchanged throughout the examinations without interval changes even during the remission phase or relapse phase (Fig. 2c, f, g). Another follow-up study in case 1 also showed no interval changes.

Swollen plexuses were not observed in any of the 11 normal volunteers. All of their plexuses showed isointensity or faintly high intensity on both STIR and T1-weighted images (Fig. 3).

Among the patients, no significant relationships were observed between MR images and clinical findings.

Measurements of ADC values

The mean ADC values in the plexuses of patients and normal volunteers were $1.27\pm0.43\times10^{-3}mm^2/s$ ($n=18$) and $0.92\pm0.11\times10^{-3}mm^2/s$ ($n=13$), respectively. The mean ADC values in patients with and without both swelling and high intensity of the brachial/lumbar plexus on STIR were $1.56\pm0.34\times10^{-3}mm^2/s$ ($n=10$) and $0.89\pm0.12\times10^{-3}mm^2/s$ ($n=8$), respectively. There were statistically significant differences between the ADC values of the patients with either swelling or abnormal signals and both normal volunteers and patients without neither swelling nor abnormal signals. However, there was no significant difference in ADC values between patients without neither swelling nor abnormal signals and normal volunteers.

Discussion

The diagnosis of CIDP is based mainly on the clinical presentation and on nerve conduction findings that are consistent with demyelination. However, in clinical practice, CIDP is often difficult to diagnose. MR examination of the brachial and lumbar plexuses will be very helpful in diagnosing CIDP.

In the present study, the MR imaging findings for nerve plexuses in CIDP patients were examined using various

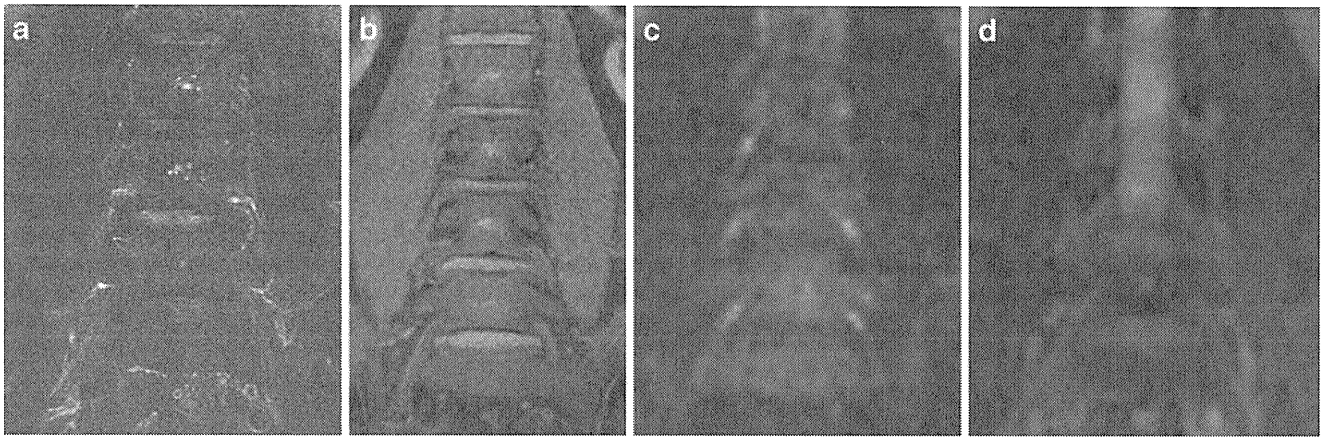

Fig. 3 MR images of a 64-year-old normal male volunteer. **a** Coronal STIR image shows the lumbar plexus without swelling or abnormal high intensity. **b** T1-weighted image shows the lumbar plexus with isointensity except for the proximal portion. **c** DWI reconstructed by MIP depicts the lumbar plexus faintly at the proximal portion. **d** The ADC value of the lumbar plexus was 1.1×10^{-3}mm^3/s

kinds of sequences, including T1-weighted images and DWIs, which had not previously been evaluated in a large number of CIDP patients. Although the most sensitive sequence for detecting signal abnormalities was STIR, T1-weighted images and DWI sequences also detected approximately 50% of the abnormalities. Moreover, high intensities on both DWI and the ADC map, which are indicative of T2 shine-through, may reflect a pathological condition in which the nerve plexus is shaped like an onion bulb.

There have been several MR studies of CIDP, some of which have shown diffuse brachial and lumbar plexus swelling and high signal intensity on T2-weighted images or STIR [5–8]. In one study, hypertrophy on MR images of plexuses in CIDP was observed in 57.1% of patients; this result is slightly lower than, but relatively consistent with the frequency observed in our study. If swelling and increased signal intensity can be detected on STIR in the plexuses of patients with clinically suspected CIDP, these findings will be of diagnostic value [6, 8].

DWIs have been investigated in several previous attempts to visualize extraspinal neural structures [10–12]. In one recent study, the quality of depiction of the brachial plexus on DWIs was evaluated [12]. The study involved five volunteers, three patients with cervical schwannoma, and two with traumatic lesions of the brachial plexus. Their study showed that DWI reconstructed by MIP provided an overview image of the brachial plexus. However, no ADC values were calculated, and the lumbar plexus was not included. Tsuchiya et al. have described the nerve roots and peripheral nerves in patients with various diseases, including three cases with CIDP, six with multiple sclerosis, and four with neurogenic tumors, using DWI [11]. They showed the affected lesion in the cord and proximal nerve roots clearly on DWI, which suggested that the DW sequence would have the potential to visualize the intramedullary and nerve root lesions, and thus facilitating a differential diagnosis. However, these studies examined several kinds of peripheral nerve diseases and included only a few CIDP cases. In addition, the ADC values were not obtained in these studies. Thus far, there have been no original MR studies with DWIs focusing on CIDP patients, nor have any studies evaluated normal brachial or lumbar plexuses on DWIs with ADC values. However, several studies have examined DWIs of normal peripheral nerves [13, 14] and have shown the normal ADC value of the median nerve to be $1.01\pm0.13\times10^{-3}$mm^2/s. Our study also demonstrated similar ADC values of the brachial and lumbar plexuses (mean $0.92\pm0.11\times10^{-3}$mm^2/s) in normal volunteers.

In this study, the DWIs showed a high signal in 55.6% of the plexuses of CIDP patients; thus, DWIs would be helpful for detecting abnormal nerve plexuses. Furthermore, patients with plexus hypertrophy had significantly higher mean ADC values than patients without hypertrophy or in the normal volunteers. Thus, the high intensity of swollen plexuses on DWIs was attributed to the T2 shine-through effect. In a study by Crino et al., the swelling of the nerve plexuses of CIDP patients was found to be caused by several proliferating layers of Schwann cells around the axon, which increased endoneurial collagen [15]. These pathological changes would explain the increased ADC values within the hypertrophic nerves. The ADC values of Schwann cell cytoplasm and endoneurial collagen surrounding bare axons in CIDP patients may be higher than those for normal myelin with tight junctions.

T1-weighted images before contrast enhancement have rarely been evaluated in CIDP patients. This study showed slightly high signal intensity in the brachial and lumbar plexuses on T1-weighted images in 50% of patients with

CIDP. During the process of re-myelination of peripheral nerves in CIDP patients, the plexus gradually becomes brighter on T1-weighted images, probably reflecting the development of the onion bulb and increased endoneurial collagen [16]. Additionally, in the course of demyelination and re-myelination, phagocytic macrophages of myelin debris are increased. Some of the lipids taken up by Schwann cells may be used to supply cholesterol for rapid membrane biogenesis by macrophages, in order to prepare for the formation of neuritis [17]. We speculate that these conditions shorten the T1 of the plexus in CIDP patients.

In the peripheral nerves of CIDP patients, increased permeability of the blood–nerve barrier appears to be the cause of spinal roots and plexus enhancement. Gadolinium enhancement has been reported in some, but not all cases of CIDP [5, 8, 10]. Midroni et al. detected the enhancement of the nerve root and the extraforaminal segment in 28.6% of cases, which was slightly lower than the 31.6% frequency observed in the present study. There has been no agreement regarding whether the enhancement of peripheral nerves indicates disease activity [7, 9]. In one of our patients who showed clinical improvement after treatment, the mild enhancement remained unchanged from before to after the treatment.

The differential diagnoses of CIDP are Charcot–Marie–Tooth (CMT) disease, distal demyelinating polyneuropathy associated with monoclonal gammopathy, and multifocal motor neuropathy (MMN). Swelling and increasing intensity on STIR with or without enhancement in nerve plexuses have also been noted in patients with distal demyelinating polyneuropathy associated with monoclonal gammopathy [5]. CMT disease, which is a hereditary peripheral neuropathy, also mimics MR findings of CIDP [18]. Because recurrent demyelination and re-myelination occur in CMT disease, the peripheral nerves often show an onion bulb as in CIDP [16]. MMN is characterized by asymmetric weakness without sensory loss. Usually, MR abnormalities are detected asymmetrically in MMN but symmetrically in CMT disease, CIDP, and distal demyelinating polyneuropathy associated with monoclonal gammopathy [19]. In particular, the affected nerve areas in CMT disease are more diffuse than in the other conditions.

Our study has several limitations. First, 12 of the 13 patients met the clinical and neurophysiological criteria for CIDP without nerve biopsy. Furthermore, in the pathologically confirmed patient, a biopsy was performed at the sural nerve and not at the plexus itself, because a biopsy at the lumbar nerve plexus carries some risks and is not usually done for the purpose of diagnosis. Although the obtained DWIs and ADC values were useful for speculating about the pathological changes in nerve plexuses in CIDP, they were not conclusive. Second, we had one follow-up study of gadolinium administration (case 9), and two follow-up studies on DWIs (cases 1 and 9). Both studies revealed no interval changes, even though one patient showed improved clinical symptoms (case 1). We think it is important for clinicians to know that there is no definite relationship between the response to treatment and any MR findings. The lack of interval changes suggests that once an onion bulb has formed, it is rarely resorbed by treatment. However, follow-up was carried out in only two patients, and a longer-term follow-up study on more patients needs to be performed.

Conclusions

Although the standard method for diagnosing CIDP includes the evaluation of clinical features and electrophysiological examinations, characteristic MR findings on STIR in CIDP patients are found to be helpful in making a diagnosis. In particular, DWIs and T1-weighted images without contrast enhancement seem useful for speculating about the pathological changes in swollen plexuses in CIDP patients.

No definite relationship was observed between MR imaging findings and clinical findings.

Conflict of interest statement We declare that we have no conflict of interest.

References

1. Hahn A, Hartung H, Dick P (2005) Chronic inflammatory demyelinating polyradiculoneuropathy. In: Dick P (ed) Peripheral neuropathy, vol 2, 4th ed. Elsevier, Philadelphia, pp 2221–2253
2. Joint Task Force of the EFNS and the PNS (2005) European Federation of Neurological Societies/Peripheral Nerve Society Guideline on management of chronic inflammatory demyelinating polyradiculoneuropathy: report of a joint task force of the European Federation of Neurological Societies and the Peripheral Nerve Society. J Peripher Nerv Syst 10:220–228
3. Latov N (2002) Diagnosis of CIDP. Neurology 59(Suppl 6):S2–S6
4. Koller H, Kieseier BC, Jander S, Hartung HP (2005) Chronic inflammatory demyelinating polyneuropathy. N Engl J Med 352:1343–1356
5. Eurelings M, Notermans NC, Franssen H, Van Es H, Ramos H, Wokke J, Van Den Berg H (2001) MRI of the brachial plexus in polyneuropathy associated with monoclonal gammopathy. Muscle Nerve 24:1312–1318
6. Bradley L, Wilhelm T, King RH, Ginsberg L, Orrell RW (2006) Brachial plexus hypertrophy in chronic inflammatory demyelinating polyradiculoneuropathy. Neuromuscul Disord 16:126–131
7. Midroni G, Tilly TN, Gray B, Vajsar J (1999) MRI of the cauda equine in CIDP: clinical correlations. J Neurol Sci 170:36–44
8. Duggins A, McLeod J, Pollard J, Davies L, Yang F, Thompson EO, Soper JR (1999) Spinal root and plexus hypertrophy in

chronic inflammatory demyelinating polyneuropathy. Brain 122:1383–1390
9. Kuwabara S, Nakajima M, Matsuda S, Hattori T (1997) Magnetic resonance imaging at the demyelinative foci in chronic inflammatory demyelinating polyneuropathy. Neurology 48:874–877
10. Tsuchiya K, Imai M, Tateishi H, Nitatori T, Fujikawa A, Takemoto S (2007) Neurography of the spinal nerve roots by diffusion tensor scanning applying motion-probing gradients in six directions. Magn Reson Med Sci 6:1–5
11. Tsuchiya K, Honya K, Yoshida M, Nitatori T (2008) Demonstration of spinal cord and nerve root abnormalities by diffusion neurography. J Comput Assist Tomogr 32:286–290
12. Takahara T, Hendrikse J, Yamashita T, Mali W, Kwee T, Imai Y, Luijten P (2008) Diffusion-weighted MR neurography of the brachial plexus: feasibility study. Radiology 249(2):653–660
13. Bendszus M, Stoll G (2005) Technology insight: visualizing peripheral nerve injury using MRI. Nat Clin Pract Neurol 1:45–53
14. Kababci N, Gurses B, Firat Z. Bayram A, Ulug A, Kovanlikaya A (2007) Diffusion tensor imaging and tractography of median nerve: Normative diffusion values. AJR 189:923–927
15. Crino B, Grossman I, Rostami A (1993) Magnetic resonance imaging of the cauda equine in chronic inflammatory demyelinating polyneuropathy. Ann Neurol 33:311–313
16. Graham I, Lantos L (2002) Greenfield's neuropathology, 7th edition, Vol. 2. New York Oxford University Press, pp 617–620
17. Naba I, Yoshikawa H, Sakoda S, Itabe H, Suzuki H, Kodama T, Yanagihara T (2000) Onion-bulb formation after a single compression injury in the macrophage scavenger receptor knockout mice. Exp Neurol 166:83–89
18. Sureka J, Charian RA, Alexander M, Thomas BP (2009) MRI of brachial plexopathies. Clin Radiol 64:208–218
19. Van Es H, Van den Berg L, Franssen H et al (1997) Magnetic resonance imaging of the brachial plexus in patients with multifocal motor neuropathy. Neurology 48(5):1218–1224

OPEN ACCESS Freely available online

PLoS one

BmDJ-1 Is a Key Regulator of Oxidative Modification in the Development of the Silkworm, *Bombyx mori*

Hiroko Tabunoki[1]*, Hiroaki Ode[1], Yutaka Banno[2], Susumu Katsuma[3], Toru Shimada[3], Kazuei Mita[4], Kimiko Yamamoto[4], Ryoichi Sato[5], Reiko Ishii-Nozawa[6], Jun-ichi Satoh[1]

1 Department of Bioinformatics and Molecular Neuropathology, Meiji Pharmaceutical University, Tokyo, Japan, **2** The Center of Genetic Resources, University of Kyushu, Fukuoka, Japan, **3** Department of Agricultural and Environmental Biology, Graduate School of Agricultural and Life Sciences, The University of Tokyo, Tokyo, Japan, **4** Insect Genome Laboratory, National Institute of Agrobiological Sciences, Tsukuba, Japan, **5** Bio-Applications and Systems Engineering, Tokyo University of Agriculture and Technology, Koganei, Tokyo, Japan, **6** Department of Clinical Pharmacology, Meiji Pharmaceutical University, Tokyo, Japan

Abstract

We cloned cDNA for the *Bombyx mori* DJ-1 protein (BmDJ-1) from the brains of larvae. BmDJ-1 is composed of 190 amino acids and encoded by 672 nucleotides. Northern blot analysis showed that BmDJ-1 is transcribed as a 756-bp mRNA and has one isoform. Reverse transcriptase (RT)-PCR experiments revealed that the BmDJ-1 was present in the brain, fatbody, Malpighian tubule, ovary and testis but present in only low amounts in the silkgland and hemocyte of day 4 fifth instar larvae. Immunological analysis demonstrated the presence of BmDJ-1 in the brain, midgut, fatbody, Malpighian tubule, testis and ovary from the larvae to the adult. We found that BmDJ-1 has a unique expression pattern through the fifth instar larval to adult developmental stage. We assessed the anti-oxidative function of BmDJ-1 using rotenone (ROT) in day 3 fifth instar larvae. Administration of ROT to day 3 fifth instar larvae, together with exogenous (BmNPV-BmDJ-1 infection for 4 days in advance) BmDJ-1, produced significantly lower 24-h mortality in BmDJ-1 groups than in the control. 2D-PAGE revealed an isoelectric point (pI) shift to an acidic form for BmDJ-1 in BmN4 cells upon ROT stimulus. Among the factors examined for their effects on expression level of BmDJ-1 in the hemolymph, nitric oxide (NO) concentration was identified based on dramatic developmental stage-dependent changes. Administration of isosorbide dinitrate (ISDN), which is an NO donor, to BmN4 cells produced increased expression of BmDJ-1 compared to the control. These results suggest that BmDJ-1 might control oxidative stress in the cell due to NO and serves as a development modulation factor in *B. mori*.

Citation: Tabunoki H, Ode H, Banno Y, Katsuma S, Shimada T, et al. (2011) BmDJ-1 Is a Key Regulator of Oxidative Modification in the Development of the Silkworm, *Bombyx mori*. PLoS ONE 6(3): e17683. doi:10.1371/journal.pone.0017683

Editor: Bob Lightowlers, Newcastle University, United Kingdom

Received October 22, 2010; **Accepted** February 8, 2011; **Published** March 24, 2011

Funding: H.T. was supported by the Ministry of Education, Science, Sports and Culture, Grant-in-Aid (http://www.jsps.go.jp/english/e-grants/grants.html) for Young Scientists (B), 2010, 22710195. This work was in part supported by grants from the High-Tech Research Center Project (http://www.mext.go.jp/english/), the Ministry of Education, Culture, Sports, Science and Technology (MEXT), Japan (S0801043), and the Research on Intractable Diseases (http://www.nanbyou.or.jp/english/index.htm), the Ministry of Health, Labour and Welfare of Japan (H22-Nanchi-Ippan-136) to J.S. The funders had no role in study design, data collection and analysis, decision to publish, or preparation of the manuscript. There was no additional external funding received for this study.

Competing Interests: The authors have declared that no competing interests exist.

* E-mail: tabunoki@my-pharm.ac.jp

Introduction

The protein DJ-1 is ubiquitously expressed in cells and it is highly conserved across a wide variety of organisms, showing moderate sequence identity with heat shock protein 31 (HSP31) chaperones and ThiJ/PfpI cysteine proteases [1]. Mutated forms of DJ-1 are known to cause early onset autosomal recessive juvenile Parkinson's disease (PD), and many studies have demonstrated a neuro-protective role of DJ-1. DJ-1, which is encoded by PARK7, is a multi-functional protein that plays roles in chaperoning, RNA-binding, SUMOylation, apoptosis, and protease activity [2].

Additionally, DJ-1 is induced by oxidative modification and is rapidly oxidized at position Cys 106 [3]. Oxidative modification leads to mitochondrial damage in cultured cells exposed to 1-methyl-4-phenyl-1,2,3,6 tetrahydropyridine (MPTP), 6-hydroxydopamine (6-OHDA), paraquat (PQ), and rotenone (ROT), which inhibit the mitochondrial electron transfer chain of mitochondrial complex I [4]. These compounds enhance production of reactive oxygen species (ROS) and reduce production of ATP, resulting in mitochondria dysfunction [5]. DJ-1 seems to directly scavenge free radicals from mitochondria in response to these oxidative stresses. MPTP, 6-OHDA, PQ, and ROT are used to produce PD models in rats and *Drosophila* and to analyze the pathology of PD [6,7].

DJ-1 has a dimer structure, and the L166P mutation produces structural perturbation that causes the protein to be ubiquitinated and susceptible to degradation by the 26S proteasome, significantly reducing its half-life *in vivo* [8,9]. L166P DJ-1 forms unstable dimers with disrupted protein folding and function [10]. The C106A mutation results in a loss-of-function of DJ-1 protease and chaperone activity [11,12]. However, the precise pathology due to mutations and species-specific biological functions of DJ-1 remain unclear.

The silkworm, *Bombyx mori*, a Lepidopteran insect, has been utilized as a model system for basic science research because of its well-characterized genome, availability of various genetic mutants, and the development of transgenic, RNAi, and microarray technologies [13,14,15,16,17]. The complete silkworm genome has approximately 18,510 genes, including a substantial number of mammalian orthologs [13,16].

In the present study, we cloned the silkworm *B. mori* DJ-1 ortholog (BmDJ-1), clarified its expression pattern during development, and examined its anti-oxidative function. BmDJ-1 is a newly identified member of the DJ-1 family and is a growth-associated protein that is altered with development in *B. mori*.

Results

Molecular cloning of BmDJ-1

Amplifying BmDJ-1 by RT-PCR with 5′ RACE using gene-specific primers from *B. mori* larvae brain cDNA produced an 86-bp product. The Kozak consensus sequence AAAATGAAG [18] was found to be present at the site of translation initiation determined using NetStart software [19]. Therefore, we determined that the cDNA encoded a putative 5′-untranslated sequence of 95 bp, an ATG start site, and an open reading frame (ORF) at position 96 extending to position 668. The deduced ORF of BmDJ-1 was composed of 672 nucleotides comprising 190 amino acids, had a molecular weight of 20,113 Dalton, and a putative isoelectric point (pI) of 5.15.

The nucleotide sequence reported in this paper has been submitted to GeneBank/DDBJ SAKURA Data bank Accession No. AB281053.

A computer search of the SMART database (http://smart.embl-heidelberg.de/) revealed that BmDJ-1 contained a DJ-1_PfpI domain at position 31T-173T. We identified the location of the BmDJ-1 gene in scaffold 2995719-2998746 of chromosome 23 at the splitting of 5 blocks by linkage mapping 28 chromosomes by SNP markers [20].

A BLAST search showed that BmDJ-1 has 50% amino acid sequence identity to *D. rerio* DJ-1 (NCBI gene ID:449674) and *D. melanogaster* DJ-1 beta (NCBI gene ID:43652); 47% amino acid sequence identity to *H. sapiens* (NCBI gene ID:11315), *X. tropicalis* (NCBI gene ID:548568), *G. gallus* (NCBI gene ID:395227), *B. taurus* (NCBI gene ID:511268), and *R. novaltis* (NCBI gene ID:117287) DJ-1; 46% amino acid sequence identity to *C. elegans* (NCBI gene ID:183625) and *M. musculus* (NCBI gene ID:57320) DJ-1; and 45% amino acid sequence identity to *D. melanogaster* DJ-1 alpha (NCBI gene ID:36543). An alignment of the deduced BmDJ-1 amino acid sequences and DJ-1 orthologs from other species using CLC Work Bench 3.2.3 showed that the BmDJ-1 protein sequence contains all of the conserved Cys and Leu residues (Fig. 1-A, black asterisks).

The phylogenetic tree placed *D. melanogaster* DJ-1 and BmDJ-1 into a distinct cluster (Fig. 1-B).

BmDJ-1 mRNA is expressed in various tissues in fifth instar larvae

Northern blot analysis revealed that there is a single transcription product for BmDJ-1 with a size of 756 bp (Fig. 2A).

We used RT-PCR to investigate the expression profile of BmDJ-1 mRNA in various tissues. BmDJ-1 showed high expression in the brain, fatbody, Malpighian tubule, ovary, and testis (Fig. 2B, upper panel lanes 2, 5–8) and low expression in the midgut, silkgland, and hemocyte (Fig. 2B, upper panel lanes 3, 4, 9).

Specificity of antibody against BmDJ-1

We examined the utility of anti-BmDJ-1 antibodies raised against the recombinant Xpress-tagged BmDJ-1 to identify BmDJ-1. Anti-BmDJ-1 antibody reacted with both recombinant BmDJ-1 protein as a 25-KDa band and BmDJ-1 in the cell and tissue lysate from *B. mori* as a 20-KDa band. In contrast, BmDJ-1 antibodies did not recognize recombinant carotenoid binding protein (CBP) from *B. mori* tagged with GST [21] and HEK 293 cell lysate (Fig. 3, lanes 1 and 4). The molecular weight of the recombinant BmDJ-1 protein (Fig. 3, lanes 2 and 3) was slightly greater than the endogenous BmDJ-1 protein (Fig. 3, lanes 5 and 6), excluding the possibility of non-specific binding to the Xpress tag.

Identification of developmental stage and tissue-specific expression patterns of BmDJ-1 by immunoblotting

Distribution of BmDJ-1 expression by developmental stage and tissue is shown in Figure 4. Whole body expression is roughly equal for all larval instars, pupae, and adults (Fig. 4A and S1A, lanes 1–7). Moreover, equal amounts of BmDJ-1 are found in the brains of fifth instar larvae, pupae, and adults, but it is slightly increased in larvae (Fig. 4B and S1B, lanes 8–10). To determine the distribution pattern of BmDJ-1, we studied tissues (midgut, fatbody, Malpighian tubule, ovary, and testis; Fig. 4C and S1C) from day 0 fifth instar larvae to adults by immunoblotting. BmDJ-1 was expressed in the larval through adult developmental stages in these tissues, but expression was low in day 1 pupae (fatbody, Malpighian tubule and ovary; Fig. 4C, panels b, c, e, lane 14). Expression levels increased with pupal stadium from day 0 to 4 (Fig. 4C, panels f–h) and high levels of BmDJ-1 expression were also identified in the testis during these developmental stages (Fig. 4C, panel q). Therefore, BmDJ-1 showed a unique day-to-day expression pattern from day 0 fifth instar larvae to the adult developmental stages.

The pI of BmDJ-1 shifted acidic by ROT stimulation

Treatment of BmN4 cells with 50 μM ROT produced a shift in the pI to acidic, as shown on 2D-PAGE and immunoblotting (Fig. 5).

BmDJ-1 overexpression in larvae causes resistance to ROT

ROT was used to produce an oxidative stress in order to examine the effect of exogenous BmDJ-1 protein. We determined the lethal dose (LD) of ROT for day 3 fifth instar larvae of 10.1 μg/g (LD_{50}; 95% CI, 6.02–17.4) (Fig. 6). Based on computer simulations of reactivity using SAS software, we determined the optimal ROT concentration for further testing of the protective effects of BmDJ-1 to be 20 μg/g.

A BmDJ-1 overexpressing silkworm produced by injecting day 0 fifth instar larvae with recombinant BmNPV-BmDJ-1 virus showed significantly decreased mortality following intrahemocoelical injection of 20 μg/g ROT after 4 days (day 3 fifth instar larvae). For three experiments, the BmDJ-1 group mortality of 38, 27, and 15% was significantly lower than mortality rates of the blank vectors (control) of 81, 93, and 90%, respectively ($P<0.01$, <0.001, <0.001, respectively; Table 1).

We also confirmed virus-derived BmDJ-1 expression levels in the fatbodies of several insects after 1 day (24 h) and 4 days (day 4 fifth instar larvae) by RT-PCR and after 4 days by immunoblotting. Expression of blank-vector recombinant virus was detected as a 300-bp band, while virus-derived BmDJ-1 expression was detected as an 850-bp band. The BmDJ-1 expression was absent at 24 h but was detected at 96 h (Fig. 7A). Virus-derived BmDJ-1 protein was expressed at about 2-fold greater levels in non-infected groups after 4 days, and BmDJ-1 protein expression in blank virus-infected control groups was significantly decreased (Fig. 7B and S2).

Expression of BmDJ-1 and NO concentration

The expression pattern of BmDJ-1 was tissue-specific, reflecting the unique responses to oxidative stress. We examined some

A

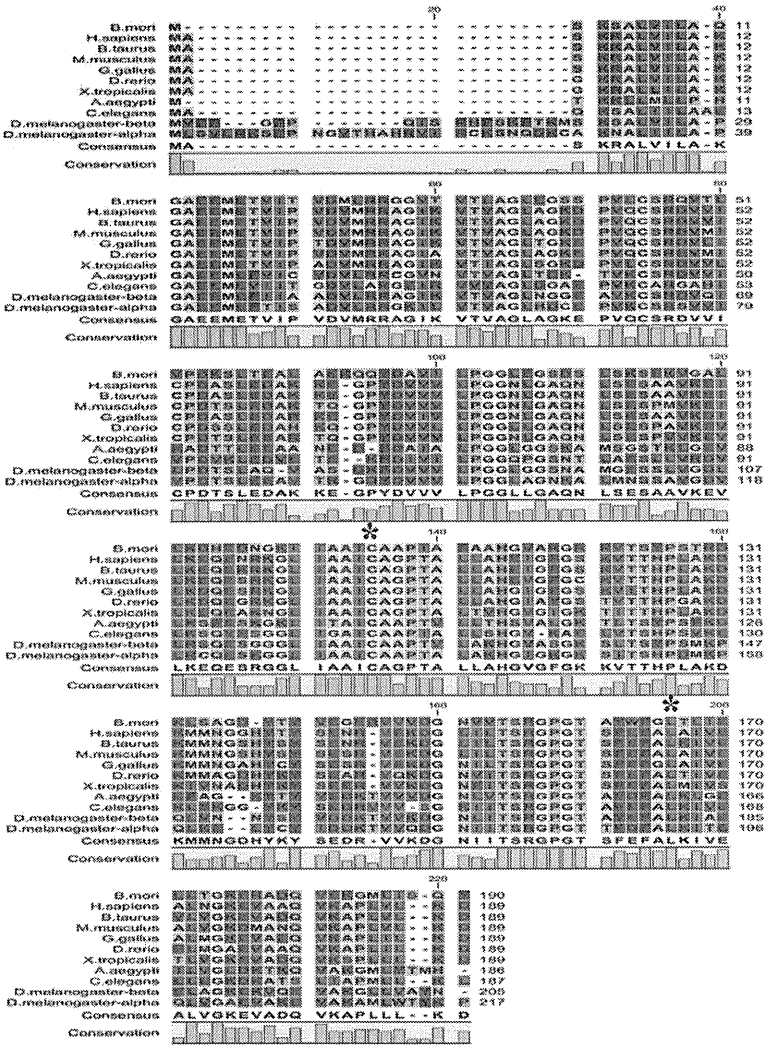
B.mori
H.sapiens
B.taurus
M.musculus
G.gallus
D.rerio
X.tropicalis
A.aegypti
C.elegans
D.melanogaster-beta
D.melanogaster-alpha
Consensus
Conservation

B

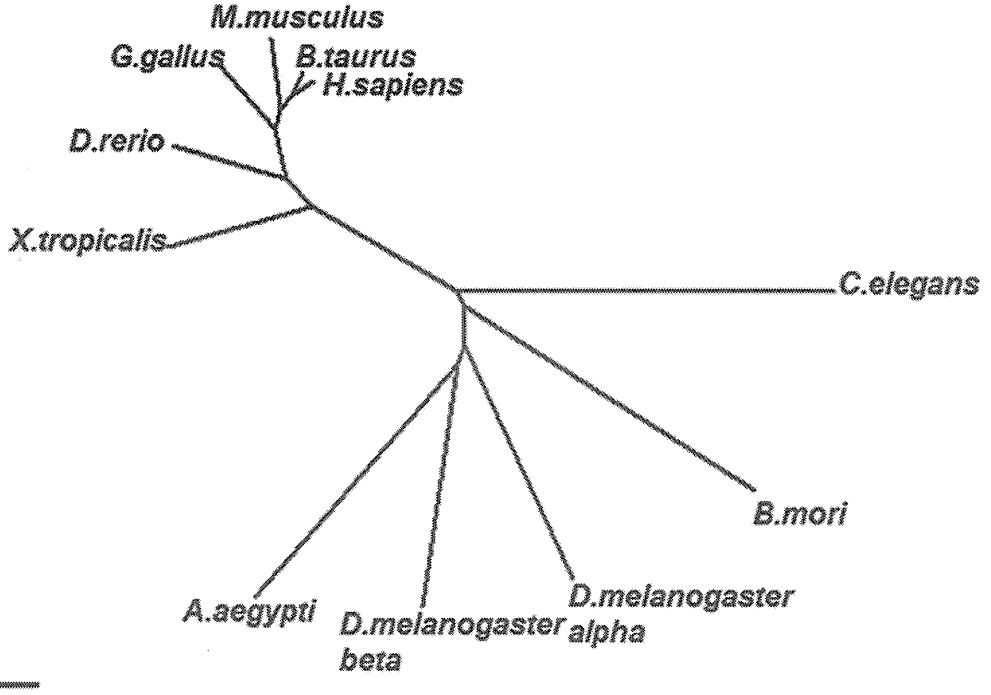
M.musculus
G.gallus
B.taurus
H.sapiens
D.rerio
X.tropicalis
C.elegans
B.mori
A.aegypti
D.melanogaster beta
D.melanogaster alpha
0.1

Figure 1. Alignment and Phylogenic tree of *B. mori* DJ-1 with other DJ-1 proteins. A. Conserved amino acid sequences C at position 106 and L at position 166 of human DJ-1 are marked by asterisks (*). The level of conserved amino acid residues among the various species are graphically shown below the sequences. The residues of the alignment are color-coded according to the Rasmol color scheme (http://life.nthu.edu.tw/fmhsu/rasframe/COLORS.HTM#aminocolors) B. The unrooted bootstrap tree of *B. mori* DJ-1 and DJ-1 protein of other species. Sequences are *Homo sapiens, Bos Taurus, Mus musculus, Gallus gallus, Danio rerio, Xenopus tropicalis, Drosophila melanogaster*-α and -β, *Caenorhabditis elegans*, and *Bombyx mori* DJ-1.
doi:10.1371/journal.pone.0017683.g001

factors that might affect expression. NO concentration in the hemolymph was found to fluctuate from the fifth instar larva to adult (Fig. 8A), with high levels for day 0 and 6 fifth instar larvae and adults and gradually increasing NO concentration in the pupal stages. To test whether NO affects the expression of BmDJ-1, BmN4 cells were treated with 100 μM ISDN as an NO donor for 16 h. BmDJ-1 was detected in each sample by SDS-PAGE and immunoblotting with NO concentration (Fig. 8B) and BmDJ-1 expression (Fig. 8C and S3) increased compared to the control (0.1% ethanol).

Discussion

Throughout its evolutionary history, DJ-1 shows a highly conserved amino acid sequence. Characterization of the *B. mori* variant, BmDJ-1, by cDNA cloning from the brains of the fifth instar larvae shows the presence of Cys and Leu, which are key residues for the function of DJ-1.

On a phylogenetic tree of DJ-1 proteins, two orthologs of *D. melanogaster*, DJ-1α and DJ-1β, and BmDJ-1 placed in distinct clusters. *D. melanogaster* DJ-1α is most highly expressed in the testis from the pupal stages to adult, and DJ-1β is expressed in almost all tissues from embryo to adult. Loss-of-function DJ-1β mutant flies are sensitive to oxidative modification from H_2O_2 and paraquat, although the role played by DJ-1α remains unclear [22]. Thus, these two *D. melanogaster* DJ-1s appear to have distinct functions.

In contrast, BmDJ-1 exists as a single isoform based on the single 756-bp transcript and only one band for BmDJ-1 on northern blot assay. The EST database (SilkBase; http://morus.ab.a.u-tokyo.ac.jp/cgi-bin/index.cgi) shows two distinct EST clones (data not shown). While BmDJ-1 may exist as several kinds of splice variants, this could not be clarified in this study.

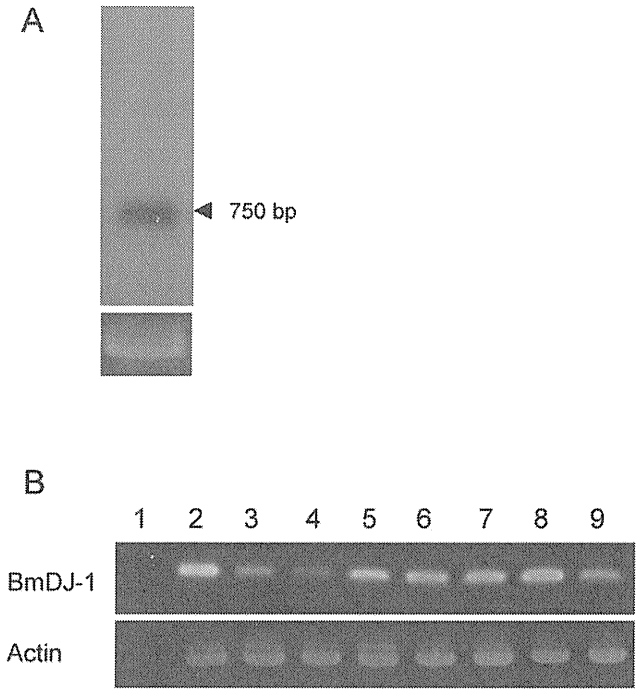

Figure 2. Northern blot analysis and RT-PCR of BmDJ-1. A. Total RNA isolated from *B. mori* ovary was analyzed by northern blot analysis using a BmDJ-1 probe. A band at about 756 bp was identified as the BmDJ-1 transcript. The amount of total RNA is 12 μg per lane. 18S ribosomal RNA was used as a control for monitoring RNA loading. B. RT-PCR for BmDJ-1 from cDNA samples synthesized from diverse larval tissues. RT-PCR for actin was used as a positive loading control and RT-PCR reaction, without reverse transcriptase, was used as a negative control. Lane 1, brain (RT-); lane 2, brain; lane 3, midgut; lane 4, silk gland; lane 5, fat body; lane 6, Malpighian tubule; lane 7, ovary; lane 8, testis; lane 9, hemocyte.
doi:10.1371/journal.pone.0017683.g002

BmDJ-1 demonstrated resistance to oxidative stress by ROT

DJ-1 has been reported to play a role in anti-oxidative stress by several independent groups. We confirmed that BmDJ-1 changes to an acidic form that is affected by ROT treatment in BmN4 cells (Fig. 5), indicating a response to oxidative stress.

In exogenous tests of BmDJ-1 with ROT, the mortality rate of individuals with BmDJ-1 is significantly decreased in the presence of ROT treatment, while the control groups remain extremely sensitive. It has been reported that the start of protein synthesis for BmNPV is 24 h after infection and that the protein expression level peaks at 96 h [23]. Endogenous protein synthesis stopped at 24 h. Immunoblotting at 96 h showed that virus-derived BmDJ-1 protein expression was significantly increased and virus-infection control group of BmDJ-1 protein expression was significantly decreased. Our findings of virus-derived BmDJ-1 expression after 96 h corroborate those results and suggest that BmDJ-1 overexpression improves the survival of silkworm larvae treated with ROT.

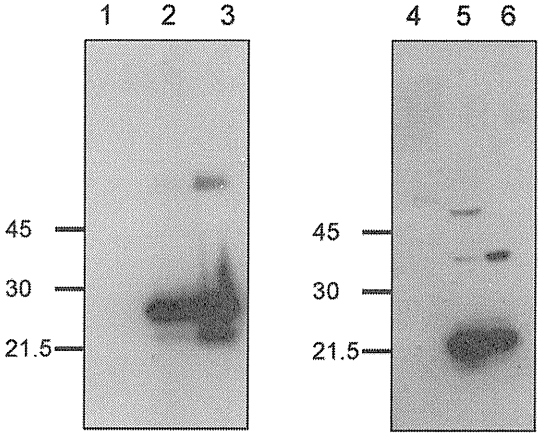

Figure 3. Specificity of anti-BmDJ-1 antibody. The recombinant protein, cell or tissue lysate were separated on a 12% SDS-PAGE gel, transferred onto a nitrocellulose membrane, and processed for immunoblotting with anti-BmDJ-1 antibody. The following samples were loaded in each lane: 1, 1 μg recombinant CBP as a negative control; 2, 0.25 μg recombinant BmDJ-1 protein; 3, 0.5 μg recombinant BmDJ-1 protein; 4, HEK 293 cells; 5, BmN4 cells; 6, larvae brain.
doi:10.1371/journal.pone.0017683.g003

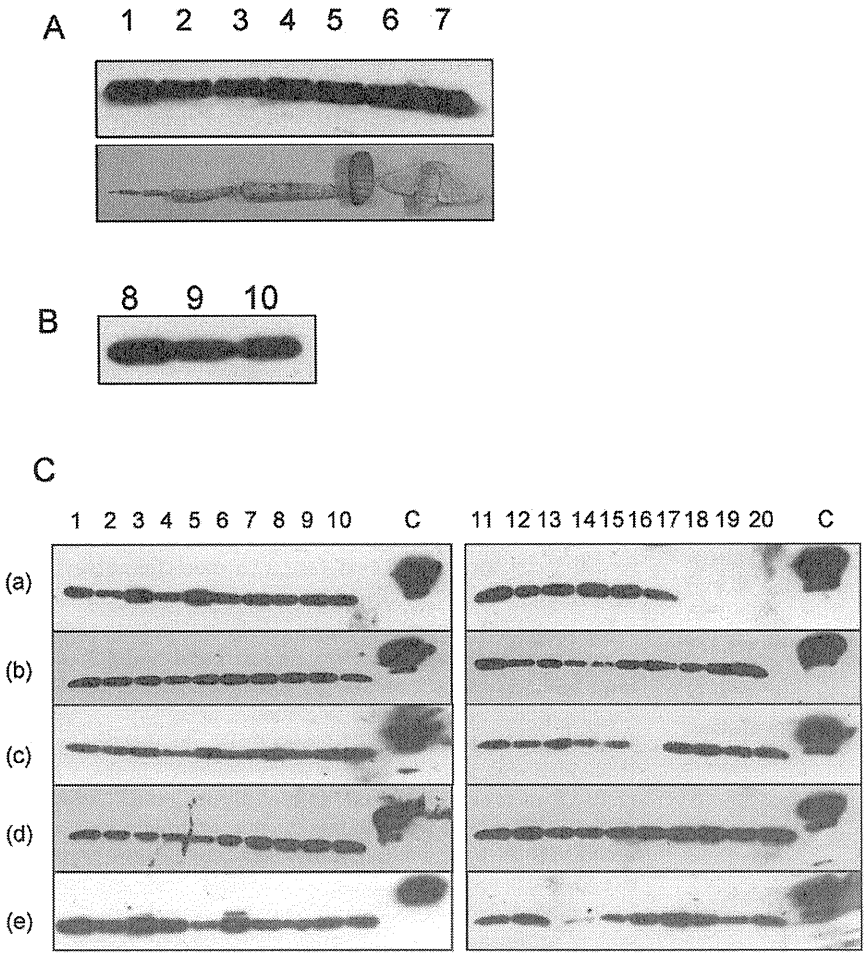

Figure 4. Developmental and tissue distribution of BmDJ-1 in *B. mori*. A. Aliquots (5 μg) of whole body homogenates from day 0 larvae of the first (lane 1), second (lane 2), third (lane 3), fourth (lane 4), and fifth (lane 5) instars, the pupae (lane 6), and the adult (lane 7) were separated by SDS-PAGE, transferred to nitrocellulose, and probed with anti-BmDJ-1 antibody. B, Aliquots (5 μg) of brain of the fifth instar larvae (lane 8), pupae (lane 9), and adults (lane 10). C. Aliquots (5 μg) of protein of various tissues were subjected to SDS-PAGE and examined for BmDJ-1 expression. The following tissues are shown: a, midgut; b, fatbody; c, Malpighian tubule; d, testis; and e, ovary were isolated from day 0 to 12 fifth instar larvae (lanes 1 to 13), from day 0, 1, 3, 4, 7 and 8 pupae (lanes 14 to 19), and from day 0 adults (lane 20). No samples were loaded in panel a, lanes 17, 18, 19, 20; panel c, lane 16; and panel e, lane 13.
doi:10.1371/journal.pone.0017683.g004

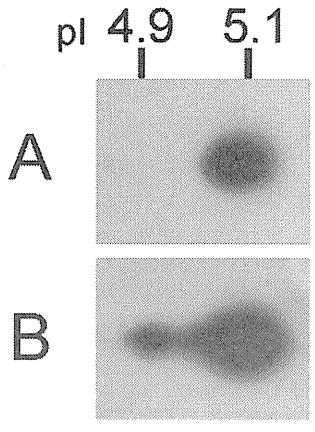

Figure 5. Effect of BmDJ-1 on ROT-induced oxidative stress in BmN4 cells. A. BmN4 cells exposed to ROT for 3 h were examined for BmDJ-1 content by 2D-PAGE and immunoblotting. A is control, B is ROT treatment.
doi:10.1371/journal.pone.0017683.g005

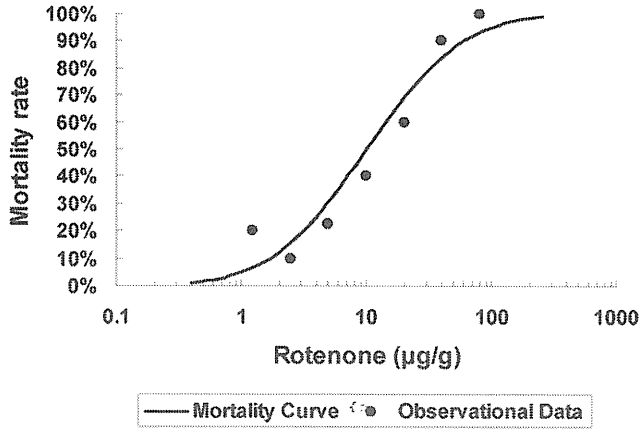

Figure 6. Dose mortality curve of rotenone in the silkworm. ROT (0, 1.25, 2.5, 5.0, 10, 20, 40, and 80 μg/g) was injected in day 3 fifth instar larvae, and the mortality rate within 24 h was examined. Filled circles were observational data.
doi:10.1371/journal.pone.0017683.g006

Table 1. Mortality rate of BmDJ-1 overexpressing (rBmNPV-infected) silkworm exposed to ROT oxidative stress.

	Silkworm mortality[a] (%)	
Experiment	Control	BmDJ-1
1	17/20 (85)	8/21 (38)**
2	14/15 (93)	4/15 (27)***
3	18/20 (90)	3/20 (15)***

[a]Rotenone (20 μg/g) was injected into BmDJ-1 overexpressing day 3 fifth instar larvae as shown in Fig. 7, and the mortality rate (dead silkworms/total silkworms; mortality rate, % in parentheses) within 24 h was examined.
**P<0.01,
***P<0.001 compared with control values.
doi:10.1371/journal.pone.0017683.t001

BmDJ-1 expression controlled with NO

BmDJ-1 showed a tissue-specific expression pattern that indicates unique responses to oxidative stress. We found that NO was an oxidative stressor in *B. mori* that could be modulated by BmDJ-1.

The BmDJ-1 expression pattern in tissues in this study suggested that BmDJ-1 expression correlates to the hemolymph NO concentration, which showed day-to-day fluctuation from fifth instar larvae to adult (Figs. 4C and 8A). Moreover, the expression of BmDJ-1 was increased and the pI shifted acidic due to exposure to an NO donor (data not shown). These results showed that BmDJ-1 was oxidized and its expression was regulated by NO.

Choi et al. [24] reported that the nitric oxide synthase (NOS) gene in *B. mori* shows the highest expression in Malpighian tubule in day 7 fifth instar larvae, suggesting that NO might be related to *B. mori* metamorphosis. Inoue et al. [25] reported that administration of ISDN, an NO donor, to the beetle *Homoderus mellyi parry* rapidly progresses pupation. Conversely, the administration of carnitine, which suppresses apoptosis of cells in larval beetles, extended the larval developmental period and generated huge adult beetles. These observations implicate NO in the mechanism of metamorphosis as an apoptosis initiator, though the underlying process remains unclear.

In *B. mori*, apoptosis is the principal mechanism for dynamic remodeling of the body structure during metamorphosis. Apoptosis mainly occurs during the pupal developmental period, during which the restructuring produces the adult body. In our observation, the increased expression levels of BmDJ-1 occur in the pupal developmental stage, which coincides with apoptosis and the apparent melting of the body. BmDJ-1 might be involved in the elimination of NO in metamorphosis.

Although DJ-1 protein acts as a controller caspase activation to alter self expression level in the apoptotic pathway [26], we cannot determine a direct relationship between BmDJ-1 and NO generation in metamorphosis based on these experiments.

In future studies, we will investigate whether BmDJ-1 directly regulates NO in metamorphosis.

Materials and Methods

Ethics statement

The study protocol for the experimental use of the animals was approved by the Ethics Committee of Meiji Pharmaceutical University (Approval ID 2004).

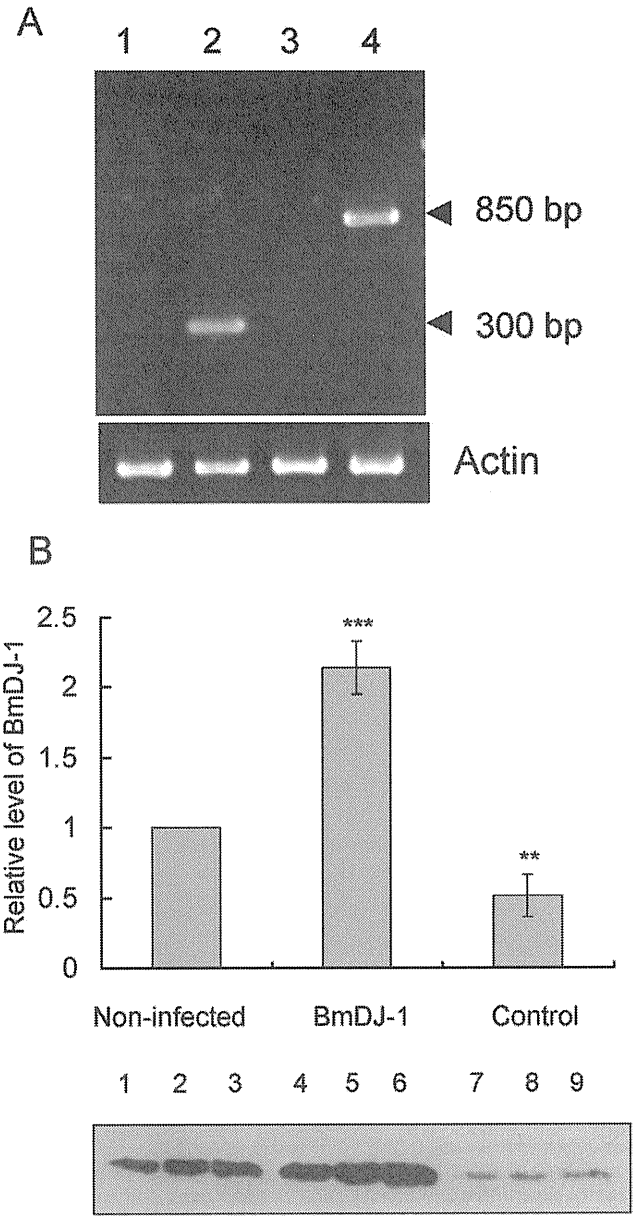

Figure 7. Expression of BmDJ-1 in silkworms infected by recombinant BmNPV. A. The fatbodies of several insects were dissected after 1 day (24 h) and 4 days (day 3 fifth instar larvae) and subjected to RT-PCR with BmNPV specific primers. Lanes 1, 2: blank virus; lanes 3, 4: recombinant virus; lanes 1, 3: 1 day after infection; lanes 2, 4: 4 days after infection. B. Aliquots (5 μg) of protein samples from fatbodies of several insects separated by SDS-PAGE, transferred to nitrocellulose, and probed with anti-BmDJ-1 antibody: non-infected control (day 3 fifth instar larvae) from experiments 1 (lane 1), 2 (lane 2) and 3 (lane 3); infected by recombinant virus from experiments 1 (lane 4), 2 (lane 5), 3 (lane 6); and blank virus after 4 days infection from experiments 1 (lane 7), 2 (lane 8), and 3 (lane 9). Protein level was measured by Image J ver 1.37 c and plotted to a graph. *P<0.05, **P<0.01 compared with control values.
doi:10.1371/journal.pone.0017683.g007

Insects

The hybrid strain Kinshu x Showa was supplied from Ueda-Sha Co. Ltd., Nagano, Japan. Individuals were reared on the artificial diet Silkmate 2S (NOSAN, Tsukuba, Japan) and kept at 25°C on a 12 h light/12 h dark daily cycle.

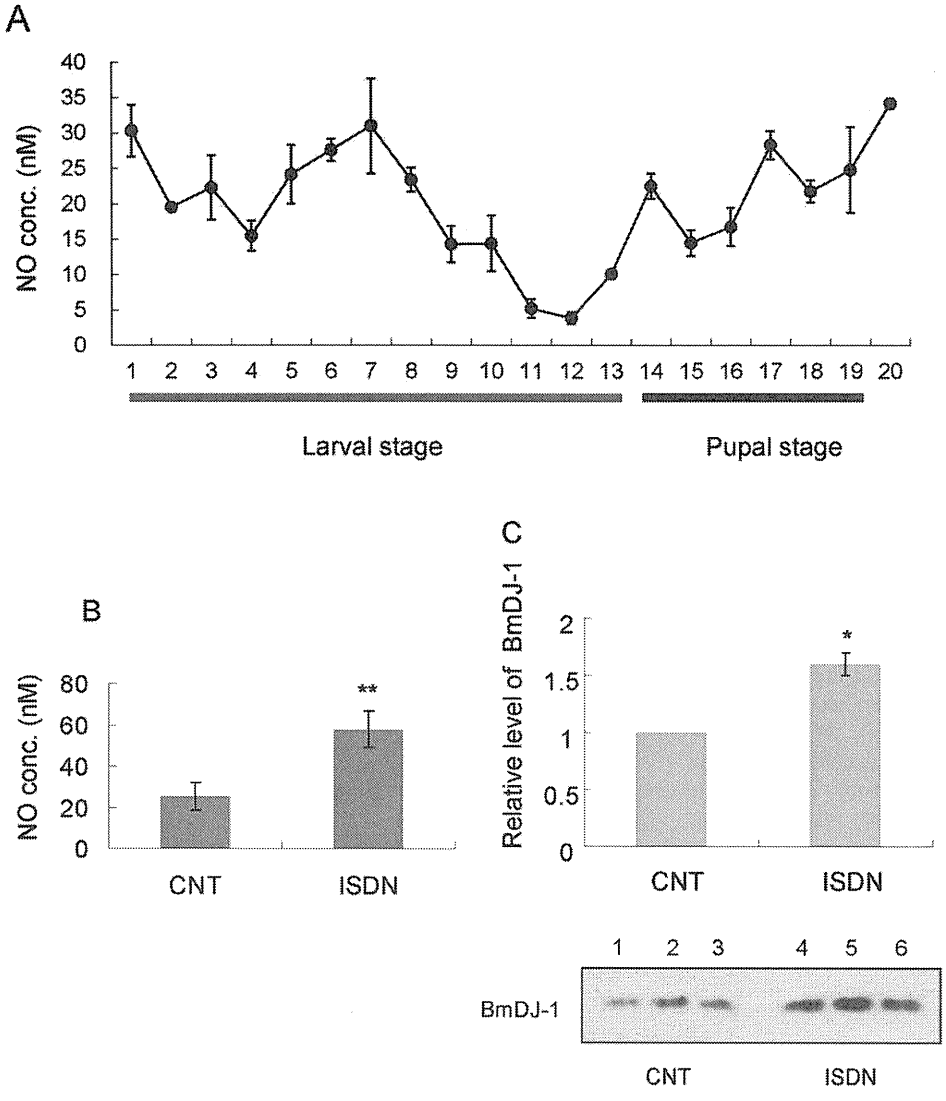

Figure 8. Change of NO concentration in hemolymph and expression of BmDJ-1 treated with ISDN. A. The hemolymph of several insects was collected from day 0 fifth instar larvae to adults and measured for NO concentration. 1–13: fifth instar larval stage (day 0 to 12); 14–19: pupal stage (day 0, 1, 3, 4, 7, 8); 20: adult. B. NO concentration in the medium. C. Aliquots (5 μg) of protein samples from BmN4 cells, experiment 1 of control (lane 1), experiment 2 of control (lane 2), experiment 3 of control (lane 3), experiment 1 of ISDN treatment (lane 4), experiment 2 of ISDN treatment (lane 5), and experiment 3 of ISDN treatment (lane 6) were separated by SDS-PAGE, transferred to nitrocellulose, and probed with anti-BmDJ-1 antibody. Protein level was measured by Image J ver 1.37 c and plotted to a graph. *P<0.05, **P<0.01 compared with control values.
doi:10.1371/journal.pone.0017683.g008

Cell culture

An established silkworm cell line, BmN4 (NOSAN), was maintained at 25°C in TC-100 medium (NOSAN) supplemented with 10% fetal bovine serum and Antibiotic-Antimycotic (Invitrogen, Carlsbad, CA, USA).

Molecular cloning of BmDJ-1

We first searched the *B. mori* expressed sequence tag (EST) database on KAIKOBLAST (kaikoblast.dna.affrc.go.jp) using the *Drosophila melanogaster* DJ-1 alpha (NM_137072) or beta (NM_143568) sequence as a query, and identified the EST clone NRPG1136, which did not overlap the 5′ end of the coding region of the *B. mori* DJ-1 gene (BmDJ-1). The entire coding sequence was determined using total RNA extracted from the brains of day 3 fifth instar larvae by an RNeasy mini kit (Qiagen, Valencia, CA, USA). DNase-treated total RNA was processed for cDNA synthesis using oligo(dT)12-18 primers and SuperScript II reverse transcriptase (Invitrogen), and cDNA was amplified by PCR using Pfu Turbo DNA polymerase (Stratagene, La Jolla, CA, USA) and the primers 5′-TCAAGAACAATGAGCAAGTCTGCG-3′ and 5′-TAATATTAGTACTGCGAGATTAAC-3′. The amplified products were cloned into a cloning vector p3T (MoBiTec, Göttingen, Germany). The purified vectors were processed for sequencing by the dideoxynucleotide chain termination method on an ABI PRIZM 3100 Genetic Analyzer (Applied Biosystems, Tokyo, Japan). The cDNA clone, NRPG1136, was provided by the National Bioresource Project (MEXT, Japan).

5′-Rapid Amplification of cDNA ends

The 5′-terminal cDNA ends were amplified using the SMART RACE cDNA Amplification kit (Clontech, Mountain View, CA, USA) according to the supplier's instructions with primers 5′-